

An investigation of the secondary load cycle associated with wave scattering in severe wave-cylinder interactions

Haoyu Ding ¹, Tianning Tang ^{2,3}, Paul H. Taylor, Thomas Adcock ², Guangwei Zhao, Saishuai Dai, Thobani Hlophe ^{2,4}, Cormac Reale and Jun Zang ¹

Corresponding author: Jun Zang, j.zang@bath.ac.uk

(Received 1 May 2025; revised 16 September 2025; accepted 19 September 2025)

This research examines in detail the complex nonlinear forces generated when steep waves interact with vertical cylindrical structures, such as those typically used as offshore wind turbine foundations. These interactions, particularly the nonlinear wave forces associated with the secondary load cycle, present unanswered questions about how they are triggered. Our experimental campaigns underscore the occurrence of the secondary load cycle. We also investigate how the vertical distributions of the scattering force, pressure field and wave field affect the nonlinear wave forces associated with the secondary load cycle phenomena. A phase-based harmonic separation method isolates harmonic components of the scattering force's vertical distribution, pressure field and wave field. This approach facilitates the clear separation of individual harmonics by controlling the phase of incident waves, which offers new insights into the mechanisms of the secondary load cycle. Our findings highlight the importance of complex nonlinear wave-structure interactions in this context. In certain wave regimes, nonlinear forces are locally larger than the linear forces, highlighting the need to consider the secondary load cycle in structural design. In addition, a novel discovery emerges from our comparative analysis, whereby very high-frequency (over the fifth in harmonic and order) oscillations, strongly correlated to wave steepness, have the potential to play a role in structural fatigue. This new in-depth analysis provides a unique insight regarding the complex interplay between severe waves and typical cylindrical offshore structures, adding to our understanding of the secondary load cycle for applications related to offshore wind turbine foundations.

© The Author(s), 2025. Published by Cambridge University Press. This is an Open Access article, distributed under the terms of the Creative Commons Attribution licence (https://creativecommons.org/licenses/by/4.0/), which permits unrestricted re-use, distribution and reproduction, provided the original article is properly cited.

¹Department of Architecture and Civil Engineering, University of Bath, Bath, BA2 7AY, UK

²Department of Engineering Science, University of Oxford, Oxford, OX1 3PJ, UK

³Department of Mechanical, Aerospace and Civil Engineering, University of Manchester, Manchester, M13 9PL, UK

⁴School of Earth and Oceans, The University of Western Australia, Crawley, WA, 6009, Australia

⁵Naval Architecture, Ocean and Marine Engineering Department, University of Strathclyde, Glasgow, G1 1XQ, UK

Key words: wave-structure interactions, wave scattering

1. Introduction

Offshore structures, including offshore wind turbines, bridge piers and floating vessels, may be subjected to severe environmental loads. Understanding the physics and statistics of wave–structure interaction, especially under nonlinear forces experienced in extreme conditions, remains a complex and partially unresolved challenge. Severe wave impacts on cylinders, for instance, can induce slam loads, addressed by various models (Von Karman 1929; Wagner 1932; Ghadirian & Bredmose 2019). Beyond these initial impacts, the interaction between waves and cylinders may generate additional strongly nonlinear forces, notably from the secondary load cycle. This phenomenon, manifesting between the crest's passage and the subsequent trough, represents a complex aspect of wave force, initially identified by Grue, Bjørshol & Strand (1993) and further explored in studies across regular wave trains (Grue & Huseby 2002), focused wave groups (Chaplin, Rainey & Yemm 1997) and irregular sea states (Stansberg 1997).

Over the years the underlying mechanisms of the secondary load cycle have been extensively debated. Tromans, Swan & Masterton (2006) advanced the discussion by subtracting the linear force from the total force to isolate the nonlinear component, showing that two distinct types of wave scattering, type-I (associated with run-up and set-down on the structure) and type-II (associated with wave diffraction around the cylinder), as identified by Sheikh & Swan (2005), contribute to the nonlinear forces that give rise to the secondary load cycle. Shortly thereafter, Rainey (2007) suggested that local wave breaking and the collapse of a cavitation bubble on the cylinder's backside might also play a role. Building on these findings, Paulsen et al. (2014) used numerical simulations to demonstrate that the strong nonlinear free-surface dynamics, in particular, the return flow from the rear of the cylinder after the passage of the wave crest, generates high-frequency force components (above the fifth and sixth harmonics) that constitute the secondary load cycle. Riise et al. (2018b) then provided a systematic experimental wave analysis, showing that, while both the Keulegan-Carpenter number and a suitably defined Froude number are important, the best correlation for the secondary load cycle magnitude is obtained with the latter, underscoring the primary role of gravity wave effects at the cylinder scale, which is also experimentally highlighted by Antolloni et al. (2020). Ghadirian & Bredmose (2020) offered a detailed force distribution using the vertical momentum equation in cylindrical coordinates, revealing that the key mechanism behind the secondary load cycle is a strong suction effect caused by the rapid downward acceleration of the water column on the rear side of the cylinder, with additional contributions from hydrostatic pressure differences and set-down effects. Rainey (2007) and Esandi et al. (2020) further underscore the potential of these nonlinear forces to trigger resonant structural responses at the natural frequencies of the system. Our new research (Tang et al. 2024) investigates the backward wave force associated with the secondary load cycle, revealing its quasiimpulsive characteristics. Despite these discussions, the precise triggers of the secondary load cycle remain elusive (Chang et al. 2019; Li et al. 2022).

In this research, we adopt the approach of Ghadirian & Bredmose (2020) for vertically distributing inline forces to analyse scattering forces, which delineate the wave force effects arising specifically from the cylinder's interactions with waves. By correlating these forces with force time histories, the scattering wave field and the scattering pressure field, we aim to clarify the mechanisms driving the secondary load cycle and its associated

nonlinear forces. With respect to the nonlinear components, wave free-surface elevations and forces, as described by the classic Stokes perturbation expansion, can be decomposed into a primary component near the spectral peak period of the incident wave and additional harmonics that arise from nonlinearities in both the incoming waves and the wave–structure interactions. These higher harmonics occur at frequencies that are approximately integer multiples of the fundamental frequency (Chen *et al.* 2018). Using a phase-based harmonic separation method (Fitzgerald *et al.* 2014), we isolate these higher harmonic components within the inline scattering force's vertical distribution, scattering pressure and scattering wave field. This method enables the precise identification of individual harmonics by combining controlled incident focused wave groups with shifted phases, thereby providing deeper insight into the nonlinear mechanisms associated with the secondary load cycle. It underscores the significance of the secondary load cycle in influencing structures subjected to severe wave interactions through a quantitative analysis of higher harmonic components. The new insights into the secondary load cycle are presented in this study.

The paper is structured as follows: § 2 introduces the experiments conducted to illustrate the occurrence of the secondary load cycle during wave-cylinder interactions, and demonstrates and validates the numerical method that provides data that are difficult to obtain from physical experiments for subsequent analysis and discussion. § 3 presents the vertical distribution of inline and scattering forces, aligned with the scattering wave field and scattering pressure field at critical time points. § 4 compares more test cases to explore the impact of wave steepness on nonlinear wave forces and the secondary load cycle. Conclusions are drawn in § 5.

2. Methodology

In this section, both experimental wave tank tests and a validated numerical method are described. We conducted 157 uni-directional focused wave groups in physical experiments, with a substantial number of tests exhibiting the secondary load cycle. In addition to the uni-directional waves, directional waves were tested experimentally and also showed the secondary load cycle. The experimental data highlight the frequent occurrence of the secondary load cycle. In parallel, our numerical method, validated against physical experiments, provides more comprehensive data on free-surface elevations of the scattering wave field, and pressure fields that are used to calculate the vertical distributions of the inline force from below to above the water's surface for the uni-directional wave regime. This analysis, based on numerical data, can offer all-around insight into the wave–structure interactions, capturing both the surface and underwater dynamics.

2.1. Physical experiments

Experiments were conducted in three facilities: the shallow water basin (35 m \times 25 m) at the Danish Hydraulic Institute (DHI) (figure 1a) (Zang, Taylor & Tello 2010; Chen et al. 2018), the towing tank (76 m \times 4.6 m) at the Kelvin Hydrodynamics Laboratory (KHL) (figure 1b) (Tang et al. 2024) and the multifunctional tank (54 m \times 34 m) at the State Key Laboratory of Coastal and Offshore Engineering, Dalian University of Technology (DUT) (figure 1c) (Ding et al. 2025). In all tests, a fixed vertical cylinder was installed. Different test scales were used: DHI tests employed a cylinder with a radius (R) of 0.125 m and a water depth (d) of 0.505 m; KHL tests used a cylinder with a radius of 0.2 m and a water depth of 1.8 m; and DUT tests featured a cylinder with a radius of 0.125 m, with water depths of 0.5 and 0.7 m. The wave generation for these experiments used focused waves based on NewWave theory (Lindgren 1970; Boccotti 1983; Tromans,

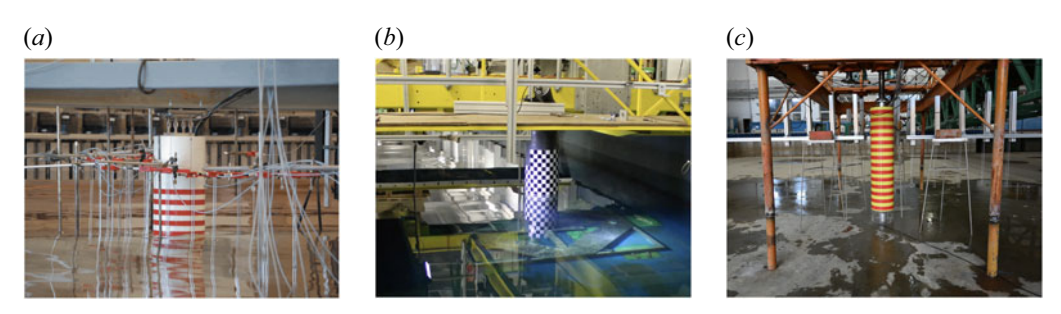


Figure 1. Set-up of experiments at (a) Danish Hydraulic Institute, (b) Kelvin Hydrodynamics Laboratory and (c) State Key Laboratory of Coastal and Offshore Engineering, Dalian University of Technology.

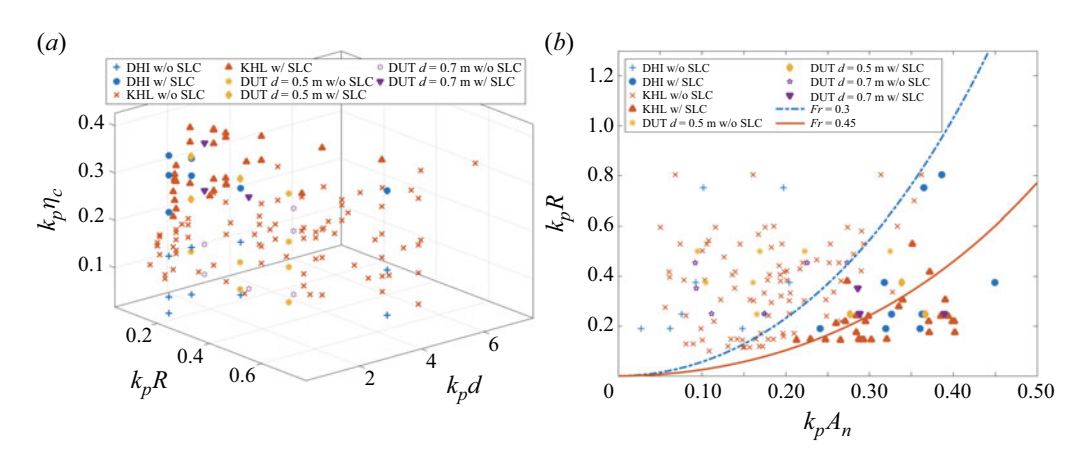


Figure 2. Occurrence of the secondary load cycle (SLC in the figure). Experimental cases are plotted in (a) with non-dimensional cylinder slenderness, non-dimensional water depth and incident wave steepness on the x-, y- and z-axes, respectively; and in (b) with incident wave steepness on the x-axis and non-dimensional cylinder slenderness on the y-axis.

Anaturk & Hagemeijer 1991) and the JOint North Sea WAve Project spectrum with a peak enhancement factor (γ) of 3.3.

2.1.1. Uni-directional waves

Figure 2(a) presents the experimental results of uni-directional wave groups, where the axes represent the non-dimensional cylinder slenderness $k_p R$, the non-dimensional water depth $k_p d$ and the incident wave steepness $k_p \eta_c$, respectively. Here, k_p is the peak wavenumber associated with the peak wave period, and η_c is the maximum surface elevation measured in the empty tank at the focus point (i.e. cylinder centre). All test cases fall within the ranges $0.10 \le k_p R \le 0.80$, $0.76 \le k_p d \le 7.24$ (intermediate to deep water) and $0.03 \le k_p \eta_c \le 0.45$. In the figure, cases exhibiting a secondary load cycle are marked with solid symbols, based on manual identification following Riise *et al.* (2018b). These cases cluster in the upper-left corner and typically correspond to larger $k_p \eta_c$.

Figure 2(b) plots experimental cases with $k_p \eta_c$ on the x-axis and $k_p R$ on the y-axis, and includes two reference lines representing Froude numbers, Fr = 0.3 and Fr = 0.45, estimated based on Riise et al. (2018a) as

$$Fr = \frac{2\pi \eta_c}{T_p \sqrt{gD}},\tag{2.1}$$

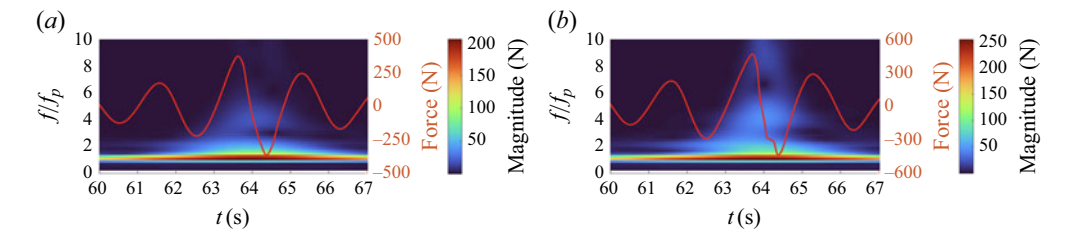


Figure 3. Force time history (in red) and wavelet contour representation of this in normalised frequency and time for KHL experiments with R=0.2 m, d=1.8 m and $T_p=1.96$ s. (a) Corresponds to $\eta_c=0.24$ m, $k_p\eta_c=0.27$, Fr=0.42 and (b) to $\eta_c=0.34$ m, $k_p\eta_c=0.37$, Fr=0.60.

where T_p is the peak wave period, g is the gravitational acceleration and D=2R is the cylinder diameter. The line at Fr=0.3, as identified by Grue $et\ al.\ (1993)$, serves as a good predictor for the occurrence of a secondary load cycle. All cases with Fr<0.3 do not exhibit a secondary load cycle, which is consistent with the prediction from Grue $et\ al.\ (1993)$. However, in some cases where Fr>0.3, no obvious secondary load cycles occur. Another line at Fr=0.45 is included to indicate the upper limit, beyond which an obvious secondary load cycle is observed in all cases; this line is also used by Tang $et\ al.\ (2024)$ as a predictor of a backward quasi-impulsive force. The experiments plotted here involve non-breaking incident waves, nevertheless, the secondary load cycle, which produces large nonlinear wave forces, occurs frequently in these non-breaking conditions.

Two experimental tests conducted at KHL (R=0.2 m, d=1.8 m) are presented in figure 3. A continuous wavelet transform is employed to analyse the evolution of the inline wave force's frequency component over time. Accordingly, figure 3 displays a contour plot of the inline force as a function of time and normalised frequency (f/f_p , where f_p is the peak incident wave frequency), with the total inline force time history overlaid in red. Figure 3(a) corresponds to the case with $T_p=1.96$ s, $\eta_c=0.24$ m, $k_p\eta_c=0.27$, $k_pR=0.22$ and Fr=0.42, whereas figure 3(b) shows the case with $T_p=1.96$ s, $\eta_c=0.34$ m, $k_p\eta_c=0.37$, $k_pR=0.22$ and Fr=0.60. In the Fr=0.60 case, an obvious oscillation appears at the trough of the total force curve at around 64 s, corresponding to the secondary load cycle. The wavelet contour reveals that the nonlinear force components ($f/f_p \ge 2$) have relatively high magnitudes (displayed in light blue) around the time of the secondary load cycle. In contrast, the Fr=0.42 case does not exhibit obvious oscillations at the trough, although nonlinear components in the frequency range from $3f/f_p$ to $5f/f_p$ are still observable around the first trough following the main crest. A similar phenomenon is also observed in the vertical distribution of the scattering force, as discussed in § 4.1.

2.1.2. Directional waves

Various directional wave spreading patterns were successfully generated in the DUT tests (Ding *et al.* 2025). The tests examined bi-directional waves, which consisted of two crossing wave groups with identical wave amplitudes and peak periods intersecting at the focus point. The crossing angles (θ) between the two wave groups were set to 40°, with each wave at $\pm 20^{\circ}$ relative to the normal to the wave paddles, respectively. For multi-directional waves, the Mitsuyasu-type spreading function $\cos^{2s}(\theta/2)$ (Longuet-Higgins, Cartwright & Smith 1963) was employed. The root-mean-square angle (σ) was set to approximately 30°, corresponding to s=7.

Figure 4 shows the incoming wave spreading pattern at the focus point in the empty tank: multi-directional waves form a hyperbolic pattern, while bi-directional waves create an X-shaped pattern. Figure 4 also compares total wave forces as functions of frequency

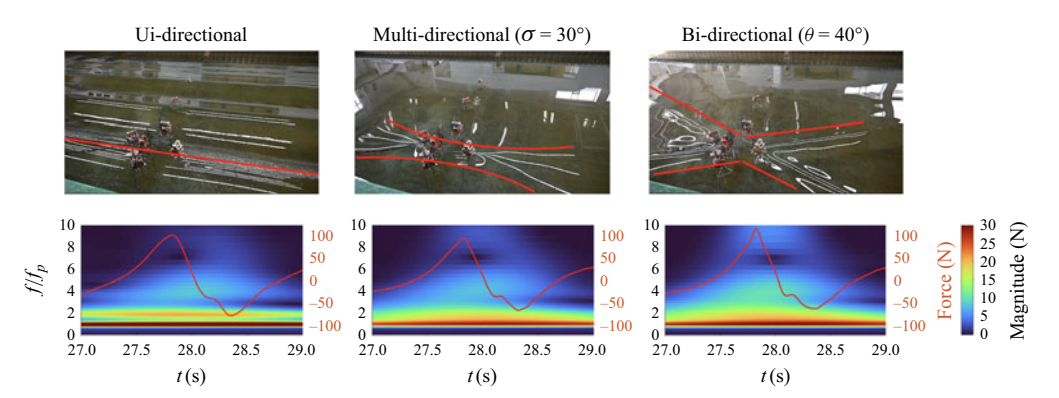


Figure 4. Wave spreading pattern in the empty tank at the focus location and corresponding wavelet analysis of inline total wave forces on the cylinder (in red) for uni-, multi- and bi-directional waves ($T_p = 1.64 \text{ s}$, $\eta_c = 0.15 \text{ m}$, d = 0.5 m) over normalised frequency and time for DUT experiments.

and time for waves with the same peak period and maximum surface elevation. Despite differences in spreading types, the wave force time histories exhibit similar magnitudes and patterns. Around 28.2 s, all wave forces show oscillations associated with secondary load cycles, with nonlinear components occurring at higher frequencies (lighter colours ranging from $3f/f_p$ to $5f/f_p$ echoing the cases in figure 3). This indicates that the secondary load cycle is observed not only in the uni-directional wave regime, most of the experimentally tested conditions, but also under physically realistic sea states with various types of directional spreading.

2.2. Numerical method

In this study, we use OpenFOAM, a computational fluid dynamics (CFD) model governed by the Navier–Stokes equations, to simulate wave–cylinder interactions, aiming to provide the wave fields and pressure fields that are necessary for evaluating the vertical distribution of the inline wave force. Previous research (Chen *et al.* 2014; Ghadirian & Bredmose 2019, 2020; Yan *et al.* 2020) has demonstrated OpenFOAM's capability to effectively simulate complex wave–cylinder interactions and predict nonlinear harmonics. We use the multiphase solver, *inter Foam*, which employs a volume-of-fluid method, to accurately track the water–air interface, and the $k-\omega$ SST model is applied for turbulence modelling.

2.2.1. Numerical wave tank set-up

The numerical wave tank, depicted in figure 5 within OpenFOAM, positions the cylinder centrally. It incorporates relaxation zones at both inlet and outlet boundaries to manage wave reflections effectively. The inlet boundary's relaxation zone is designed to absorb waves reflected off the cylinder, whereas the outlet boundary's relaxation zone mitigates incident wave reflections. Following the recommendations of Jacobsen, Fuhrman & Fredsøe (2012), both zones extend $1.5 \times$ the wavelength of the incident waves, ensuring near complete wave attenuation. This strategic configuration allows the total length of the numerical wave tank to be significantly shorter than the physical wave tank and without the influence of reflected waves. The wave tank's total length is set to $7 \times$ the wavelength of the incident waves. Wave generation is achieved by specifying wave parameters at the inlet boundary, utilising the waves2foam toolbox (Jacobsen *et al.* 2012).

Figure 5 also illustrates the mesh surrounding the cylinder in OpenFOAM. Chen *et al.* (2014) carried out a comprehensive series of mesh convergence tests to identify the optimal

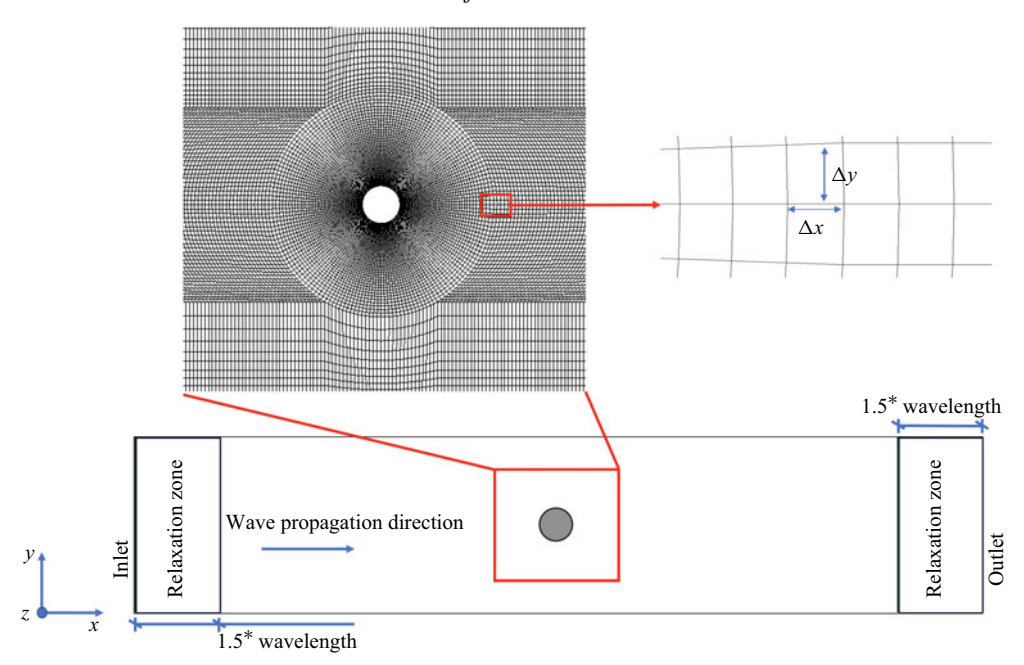


Figure 5. Top view of the numerical wave tank set-up and mesh configuration in OpenFOAM.

mesh size for accurately simulating wave–cylinder interactions. We employ the same specifications for the outermost layer of mesh cells, with horizontal mesh sizes Δx and Δy set to L/140, and vertical mesh size Δz to A/8. Here, Δx and Δy are the horizontal mesh dimensions and Δz is the vertical mesh dimension, as depicted in figure 5. The parameter L represents the incident wavelength, and A denotes the incident wave amplitude. In this study, we further refine the mesh by reducing the horizontal width Δx of the innermost layer around the cylinder to $0.2 \times$ the thickness of the outermost layer. This adjustment is crucial for capturing complex and localised wave behaviours with good accuracy, such as the steep gradient of wave run-up on the cylinder and the secondary load cycle. In addition, the numerical wave tank in Chen *et al.* (2014) exploited lateral symmetry and modelled only half of the domain along the tank centreline to reduce computational cost. In the present study, the entire domain is retained (figure 5) so that any asymmetries that may arise under severe wave conditions are fully captured.

2.2.2. Validations

This section validates our numerical model using experiments conducted at DUT. In our simulations, we replicate the DUT test conditions by maintaining the same scale and dimensions for the cylinder (R = 0.125 m) and water depth (d = 0.5 m for this validation). Our model effectively captures the nonlinear evolution observed in steep wave groups propagating along the wave tank, which is a phenomenon corroborated by Lo & Mei (1985) and Baldock, Swan & Taylor (1996). To ensure fidelity to experimental conditions, we first performed an empty wave tank test in the CFD model (without the cylinder) to verify that the initial wave conditions closely match those generated in the experiments.

Figure 6 compares CFD simulations with experimental measurements of the freesurface elevation at the focus point (also the cylinder centre). The test wave has a peak period of $T_p = 1.64$ s and a main crest amplitude of $\eta_c = 0.14$ m, resulting in $k_p \eta_c = 0.28$, $k_p d = 0.99$ and $k_p R = 0.25$, which indicate steep wave conditions. Overall, the CFD

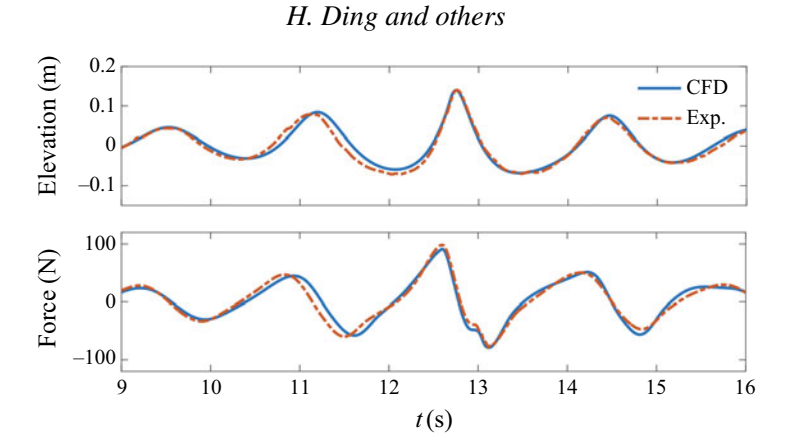


Figure 6. Comparisons of CFD results with DUT experimental measurement showing time histories of elevation (the free-surface elevation at the focus point in an empty wave tank) and force (the total inline force on the cylinder).

results show good agreement with the experimental data. Although minor discrepancies appear between 11 and 12 s, the main crest and its subsequent trough, which are critical to the secondary load cycle, are well captured. Moreover, the total inline wave force predicted by CFD aligns with experimental results, with both displaying a distinct oscillation around 13 s associated with the secondary load cycle under steep wave conditions.

Figure 7 provides a zoomed-in comparison from 12.5 to 14 s during the main crest's passage. Both the incident free-surface elevations and the total inline force exhibit excellent local agreement between CFD simulations and experiments. The secondary load cycle, indicated by the nonlinear force components, is accurately reproduced by the CFD model. Additionally, the pressure data used to calculate the vertical distributions of the inline force are validated in figure 7. Unlike the total force, which is an integrated result, point pressure measurements present a more refined challenge due to their sensitivity and the complexity involved in their prediction. Three points are compared: P1 is at the cylinder's front stagnation point, with Z = 0, where Z indicates the relative height from the still water level, while P2 and P3 are at 0.1 m below the still water level and positioned 100° and 140° from the frontal stagnation point, respectively. The two underwater point pressures show good agreement between CFD results and experimental data. A small local oscillation around 13 s is even captured by the CFD model at P2 and P3. Although CFD slightly overestimates the P1 peak value, the duration of the crest corresponding to the wave run-up interaction time is well predicted by the CFD model.

In summary, the CFD model described in § 2.2.1 accurately reproduces wave—cylinder interactions while preserving key nonlinearities. These validations establish the reliability of our subsequent analyses and discussions.

3. Secondary load cycle analysis

In continuation of our previous work, the example case presented in this section is conducted at the same scale as the KHL experimental tests and the numerical set-up described in Tang *et al.* (2024). Uni-directional focused wave groups are used for all the following investigations. The focused wave group in this section features a maximum free-surface elevation measured at the focus point (η_c) of 0.41 m, a peak wave period (T_p) of 2.52 s, a water depth of 1.8 m and a peak wavenumber associated with the peak wave

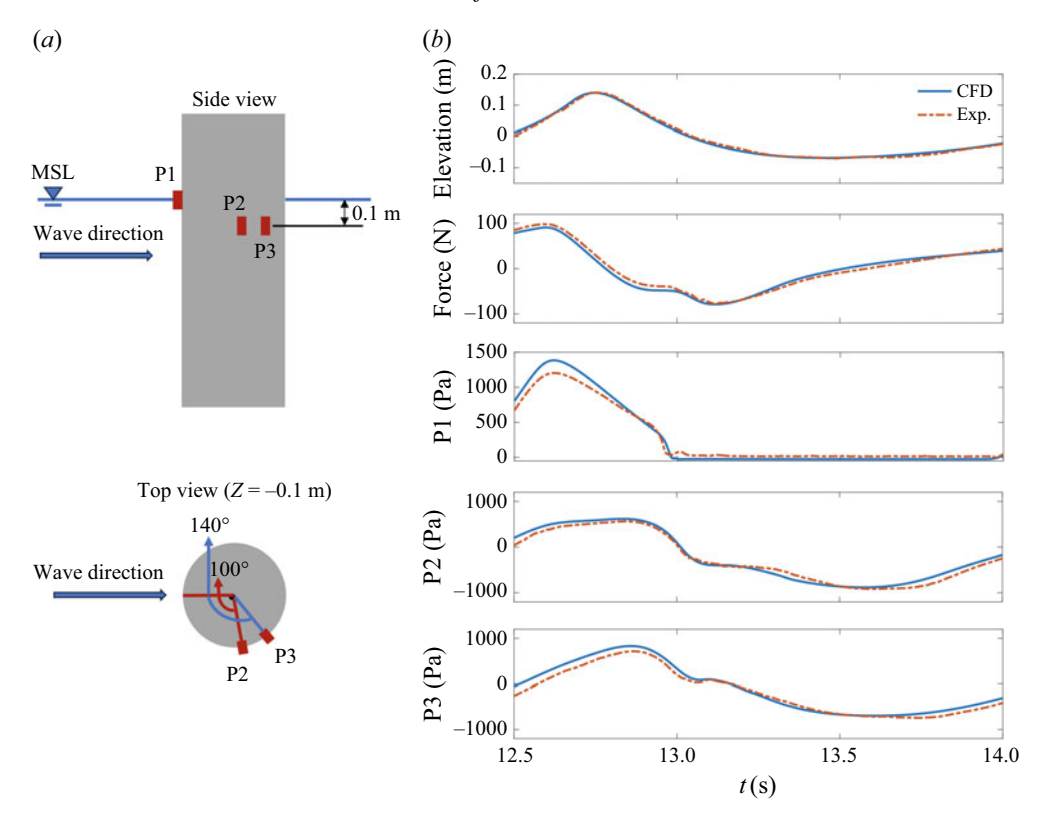


Figure 7. (a) Set-up of point pressure probes on the cylinder's surface, where MSL refers to mean sea level. (b) Zoomed-in comparisons of CFD results with DUT experimental data showing time histories of elevation (the free-surface elevation at the focus point in an empty tank), force (the total inline force on the cylinder), P1 (the point pressure at the cylinder's front stagnation point, with Z = 0, where Z indicates the relative height from the still water level), P2 (the point pressure at 0.1 m below the still water level and positioned 100° from the frontal stagnation point) and P3 (the point pressure at 0.1 m below the still water level and positioned 140° from the frontal stagnation point).

period (k_p) of 0.73 m⁻¹. These parameters result in a local wave steepness measured at the focus point $(k_p\eta_c)$ of 0.30 and a cylinder slenderness (k_pR) of 0.15.

3.1. Inline force per unit vertical length

The inline force per unit vertical length is derived from the circumferential integration of local point hydrodynamic pressure, aligned with the inline direction. This is visualised in a contour plot against time and along the cylinder's height Z in figure 8, where Z=0 corresponds to the still water level, and Z<0 signifies submersion. Notably, a positive value of the force per unit vertical length signifies a force direction that aligns with the incident wave's propagation direction, whereas a negative value denotes a force direction opposing the wave's approach (this approach of the force direction definition will be applied to all the results in this research).

Between 12 and 14 s, coinciding with the crest and trough of the total force, the contour plot of the inline force per length reveals a positive region when the force peaks and a negative region during the trough, delineated by a distinct boundary. After 14 s, the total force tends to the main crest, corresponding to pronounced magnitudes in the inline force per length prior to 15 s. The secondary load cycle is apparent in the total force trace near

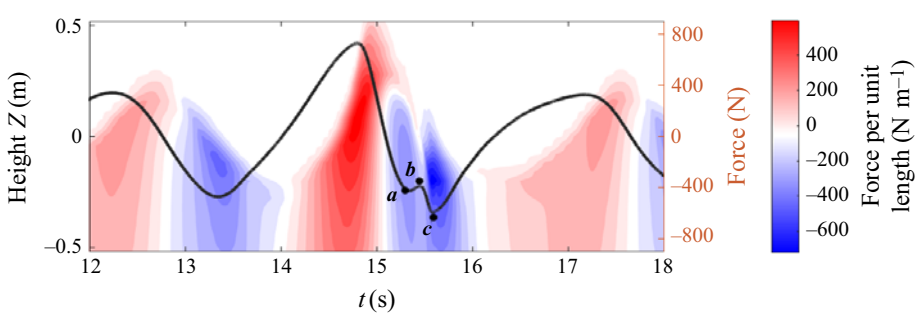


Figure 8. Contour plot of inline force per unit vertical length against vertical level relative to still water level and time, with overlaying time histories of total force (black line). Critical time points a (15.30 s), b (15.45 s) and c (15.60 s) are highlighted.

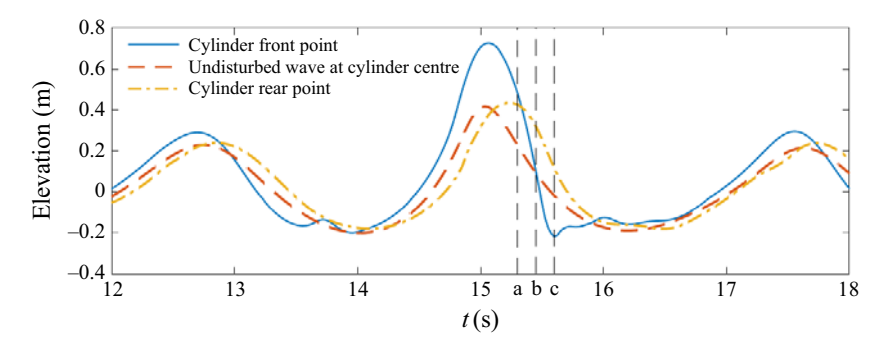


Figure 9. Time histories of free-surface elevations at the cylinder's front and rear stagnation points during wave-cylinder interactions, alongside time histories of undisturbed free-surface elevation at the planned cylinder centre measured in an empty tank.

15.5 s. In the contour plot of the inline force per length, a notable negative 'chamber' forms beneath the positive region at Z=0.2 m, approximately at 15 s, indicating the onset of the secondary load cycle. At point a, marked at 15.30 s on the total force–time history curve, a shift towards a positive tendency begins. Contrasting with the period between 12 and 14 s, which exhibits a distinct boundary, a positive region, named a 'positive insertion', transiently inserts into the negative zone as a minor crest appears in the trough of the total force, succeeded by a pronounced negative region around Z=-0.2 m. Here, the 'positive insertion' indicates the peak of the oscillation associated with the secondary load cycle, while the subsequent significant negative area represents the quasi-impulsive force at the trough of the total force–time history curve, as discussed in our previous study (Tang *et al.* 2024). Additionally, two pivotal points are identified as point b and point c at 15.45 and 15.60 s, respectively.

Free-surface elevations at three locations along the central line in the direction of wave propagation around the cylinder are shown in figure 9. Elevation time histories are taken at the front stagnation point of the cylinder, the undisturbed wave at the planned centre point of the cylinder in an empty tank (i.e. the free-surface elevation at the focus point), and the rear stagnation point. Notably, the front stagnation point exhibits a significantly higher peak crest in its free-surface elevation, highlighting substantial wave run-up at the cylinder's front when compared with undisturbed waves. Meanwhile, at the rear stagnation point, despite the cylinder's presence, the peak free-surface elevation marginally exceeds that of the undisturbed waves, attributed to wave diffraction.

Critical time points a, b and c, identified in figure 8, are also marked in figure 9. These correspond to: the intersection of front and rear stagnation point elevations at point a (15.30 s); the intersection of the front stagnation point elevation with the undisturbed wave elevation at point b (15.45 s); and the trough of the front stagnation point elevation at point c (15.60 s), which coincides with the quasi-impulsive force observed from the rear of the cylinder in figure 8. At point c, the notable wave set-down in front of the cylinder potentially amplifies the negative force, offering insights into the occurrence of the quasi-impulsive force. However, the free-surface elevations at points a and b do not match the timings of the emergence of the oscillation or the negative 'chamber' beneath the positive region, nor the peak of the oscillation or the 'positive insertion'. Therefore, a detailed discussion on the three-dimensional wave field surrounding the cylinder is warranted in subsequent sections to fully comprehend the nonlinear inline force phenomena.

3.2. Scattering force per unit vertical length

The scattering pressure is calculated by subtracting the baseline pressure (measured in the absence of the cylinder but with the same incident wave group) from the total pressure recorded when the cylinder is present. To achieve this, point pressure measurements are collected from the surface of a cylinder within the CFD simulation. Correspondingly, point pressure is also measured at the same location in an empty wave tank, to capture the pressure contributions from incident waves alone. The difference between these two measurements yields the scattering pressure, which represents the pressure changes attributable solely to the cylinder's interaction with the waves. Employing these scattering pressures, we can obtain the scattering force per unit vertical length (hereafter, SFL), as shown in figure 10. Following a similar principle for deriving the scattering pressure, the scattering wave field, also presented in figure 10, is obtained by subtracting the free-surface elevation measured in the empty tank from that measured during the cylinder's interaction with the wave. This approach enables a detailed examination of how the presence of the cylinder influences the wave forces and the wave profiles in its vicinity.

Figure 10 illustrates the SFL, highlighting three critical points: a (15.30 s), marking the onset of the secondary load cycle (corresponding to the negative 'chamber' in the SFL); b (15.45 s), located at the peak of the oscillation associated with the secondary load cycle (denoted as the 'positive insertion' in the SFL); and c (15.60 s), pinpointing the quasi-impulsive force at the trough in the total force-time history (leading to a significant negative region in the SFL). These critical points are marked on the curve representing the total force, alongside scattering wave free-surface elevations measured at both the front and rear stagnation points of the cylinder. The alignment of total force curves with the SFL over time histories reveals that the SFL mirrors the distribution of positive and negative regions found in the total inline force per unit vertical length, as depicted in figure 8. Notably, in the SFL, the 'positive insertion' not only occurs concurrently but is also more distinctly observable and exhibits a significantly greater magnitude than seen in the total inline force per unit vertical length. This observation underscores that the 'positive insertion' is primarily driven by scattering forces. Moreover, although the pronounced negative region following the 'positive insertion' in the SFL displays a relatively lower magnitude compared with the total inline force per unit vertical length, approximately $-530 \text{ N m}^{-1} \text{ versus } -700 \text{ N m}^{-1} \text{ at } 15.6 \text{ s, it still dominates this phenomenon.}$

The scattering wave field around the cylinder at time points a (15.30 s), b (15.45 s) and c (15.60 s) is depicted in figure 10. A supplementary movie of the full evolution from 12 to 18 s (Movie 1) is available at https://doi.org/10.1017/jfm.2025.10738. At 15.30 s, a wave run-up is observed at the cylinder's front, aligned with the direction of the incident wave,

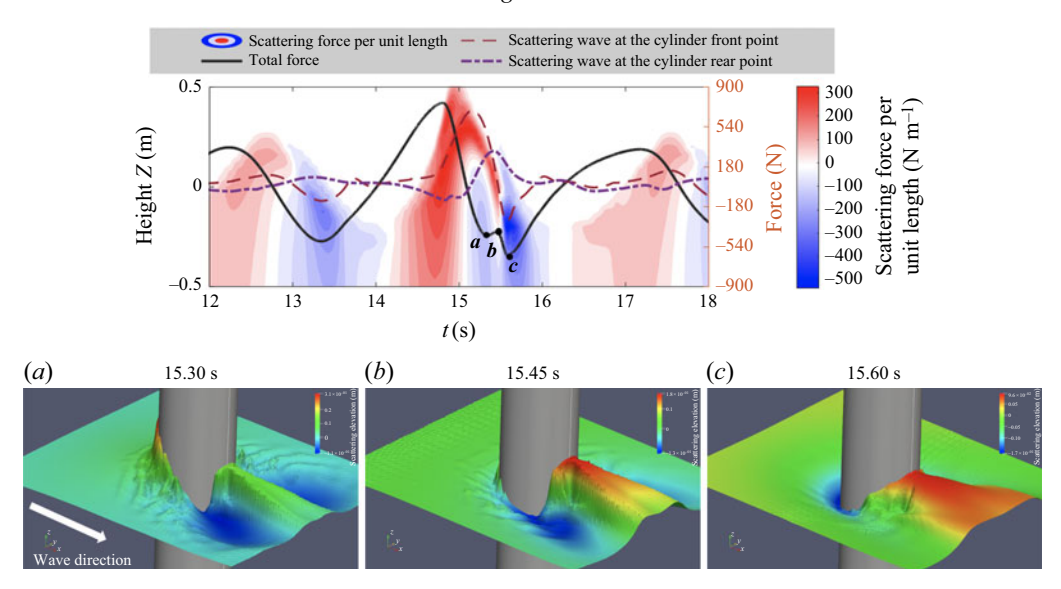


Figure 10. Contour plot of inline SFL against vertical level relative to still water level and time, with overlaying time histories of total force (black line). Also depicted are the scattering wave free-surface elevations at the cylinder's front stagnation point (red dashed line) and the rear stagnation point (purple dash-dot line). The scattering wave field around the cylinder is shown at three time points: (a) 15.30 s, (b) 15.45 s and (c) 15.60 s. (Colour bar in the scattering wave field: scattering elevation (m).)

and this run-up is in a set-down phase, as indicated by the scattering wave free-surface elevation time histories in figure 10. Conversely, at the cylinder's rear, the wave set-down is evident on both shoulders, while a ridge-type wave run-up occurs at the rear stagnation point.

Figure 11 illustrates the distributions of SFL on the front and rear halves of the cylinder, where the overall SFL depicted in figure 10 constitutes the sum of these distributions. Specifically, figure 11(a) shows that wave run-up corresponds to positive force, while wave set-down induces negative force. Conversely, in figure 11(b), wave run-up produces a negative force and wave set-down aligns with a positive force. At 15.30 s, the front side distribution shows a positive value around the free surface, corresponding to the frontal wave run-up and contributing a positive force in the direction of wave propagation. On the rear side, positive values near the free surface are also observed. Although the wave run-up at the rear stagnation point, contrary to the frontal wave run-up that contributes a positive force, tends to generate a negative force, the suction due to the wave set-down occurring on the rear shoulders exerts force in the positive direction. This finding aligns well with observations by Ghadirian & Bredmose (2020) regarding a strong suction effect at the cylinder's rear side. This combination of run-up and suction results in a positive SFL near the free surface on the rear side, as shown in figure 11(b).

However, the negative 'chamber' beneath the positive region in the SFL is not directly evident from the scattering wave profile at 15.30 s. By comparing the SFL distribution from 12 to 14 s in figure 10, we can infer that the negative region is a natural evolution following the wave crest's passage, with the total force transitioning from positive to negative around 15 s. The 'chamber' appearance in the SFL is due to the emergence of a positive region near the free surface, leading to the 'positive insertion'. This presence mitigates the rate of decrease in the total force's tendency towards the negative trough, even reversing it towards a positive direction at 15.30 s, thereby initiating the secondary load cycle's oscillation.

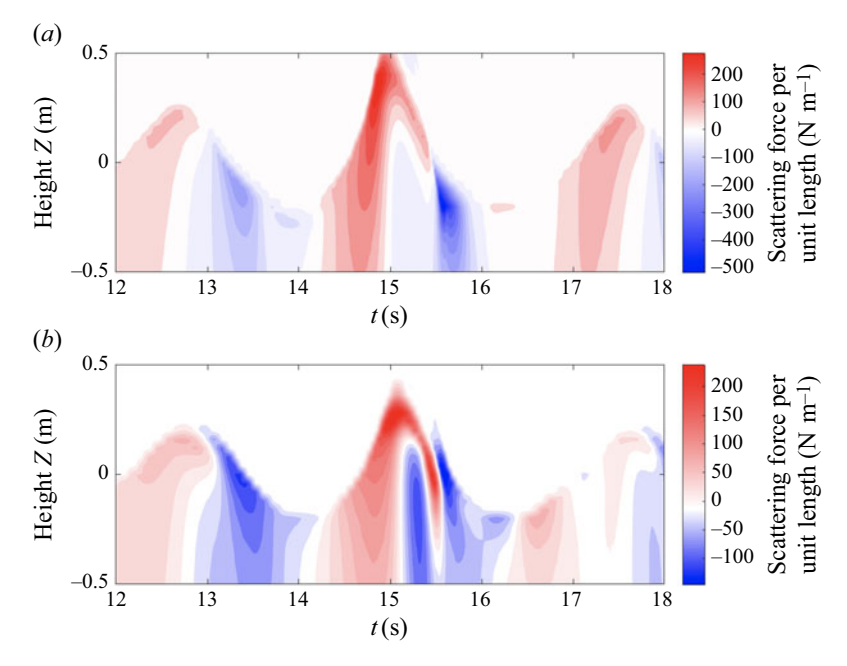


Figure 11. Contour plot of scattering inline force per unit vertical length against vertical level relative to still water level and time, showcasing (a) the front side and (b) the rear side distributions.

From 15.30 to 15.45 s, the wave run-up at the front of the cylinder continues to set-down, yet remains above the average free-surface level. Consequently, the front side distribution of SFL, depicted in figure 11(a), exhibits a positive value of approximately 50 N m⁻¹ near the free surface. In contrast, the rear side distribution, shown in figure 11(b) at 15.45 s near the free surface, reaches over 210 N m⁻¹, significantly influencing the 'positive insertion' observed in the overall SFL in figure 10. This dominance of the 'positive insertion' by the rear side's force is mirrored in the scattering wave field at 15.45 s. Similar to the observations at 15.30 s, the positive forces at this time are attributed to the suction effects of the wave set-down on both rear shoulders of the cylinder. Notably, the depth of the lowest set-down has deepened to -0.13 m at 15.45 s from -0.11 m at 15.30 s, indicating a progression in the wave set-down phenomenon. These same features were first described by Grue *et al.* (1993).

Sheikh & Swan (2005) identified a scattering wave field linked to water motion around a cylinder. The presence of the cylinder disturbs the water's surface, with one part producing the run-up and set-down, known as the type-I scattering wave, and another part, termed the type-II wave, increasing elevations along both sides. This type-II wave disturbance eventually forms a distinct mound on the rear face, which then propagates around the cylinder's surface toward the upstream side before apparently being released from the cylinder.

At 15.60 s, a type-II scattering wave emerges from behind the cylinder. At this time, the wave run-up at the cylinder's front has set-down to its lowest point, as evidenced by the scattering wave free-surface elevation at the front stagnation point. This set-down contributes to the generation of negative forces, as depicted in the front distribution of SFL shown in figure 11(a). Concurrently, the wave set-down previously observed on the rear shoulder has vanished by 15.60 s, leaving behind only the wave run-up at the cylinder's rear. This run-up also results in negative forces, as illustrated in the backside

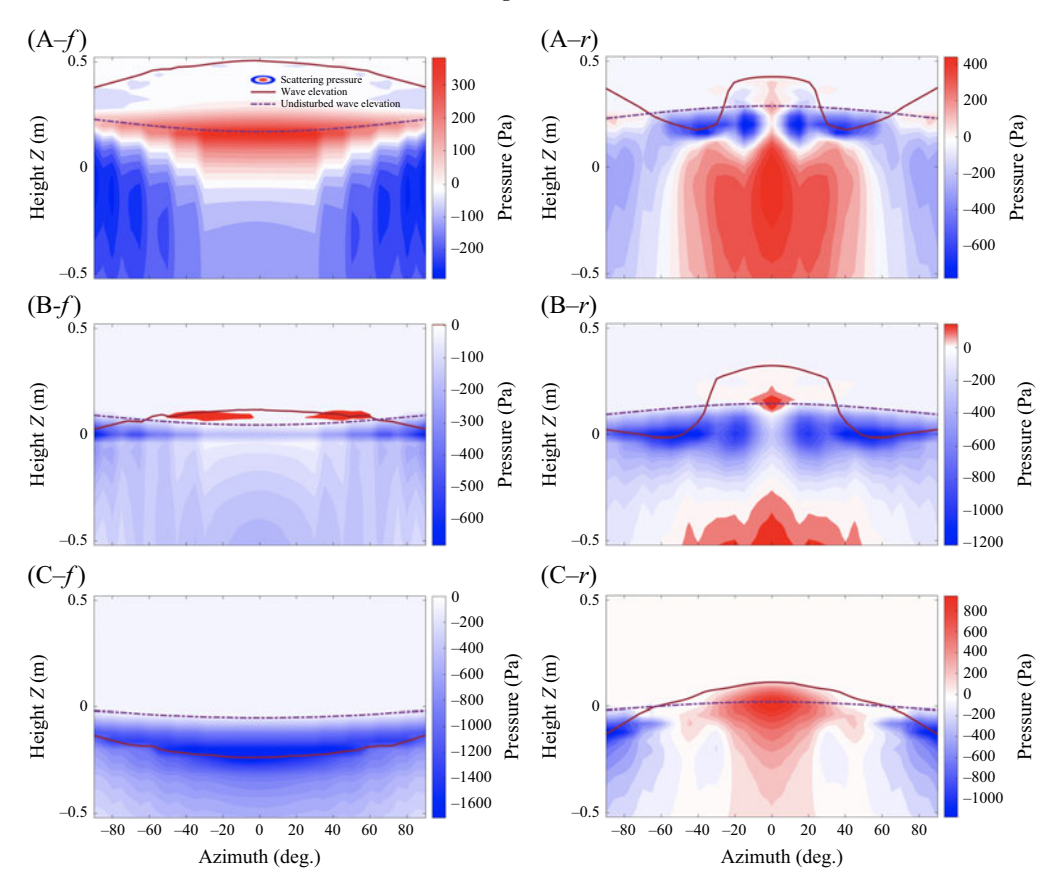


Figure 12. Contour plot of scattering pressure against cylinder height and azimuth at time point a (15.30 s), showcasing (A-f) the front side and (A-r) the rear side, at time point b (15.45 s) showcasing (B-f) the front side and (B-r) the rear side and at time point c (15.60 s) showcasing (C-f) the front side and (C-r) the rear side.

distribution of SFL in figure 11(b). The combined effects of the front and rear side distributions lead to a pronounced negative region, culminating in a quasi-impulsive force at the trough in the total force curve. The elevation differences between the frontal wave set-down and the backward wave run-up are distinctly captured in the respective front and backside distributions of the SFL, underscoring the dynamic interplay of forces at work.

3.3. Azimuthal scattering pressure

To calculate the SFL in § 3.2, the scattering pressure, which represents the pressure changes attributable solely to the cylinder's interaction with the waves, is used. Figure 12 presents the azimuthal distribution of scattering pressure, corresponding to the SFL shown in figure 10. These figures highlight critical points on the cylinder surface where significant scattering pressure is induced by wave scattering around the cylinder.

In figure 12, the front and rear sides of the cylinder are presented separately. On the front side, the front stagnation point is defined as 0° azimuth. Moving counterclockwise, the azimuth reaches -90° at one cylinder shoulder and 90° at the opposite shoulder.

Conversely, on the rear side, the rear stagnation point is set at 0° azimuth, with the azimuth increasing clockwise from -90° at one shoulder to 90° at the other.

Figures 12(A-f) and 12(A-r) show the azimuthal scattering pressure at time point a (15.30 s). The free-surface elevations of the wave interacting with the cylinder around its circumference and the undisturbed wave elevation in an empty tank at the same locations are also presented alongside the contour plot of the scattering pressure. At 15.30 s, the main crest peak has passed the cylinder location, and the main crest of the focused wave is moving past the cylinder, as observed from the undisturbed wave at the cylinder centre in figure 9. Consequently, the azimuthal undisturbed wave elevation at the front stagnation point is at the lowest water surface level, and as one moves around the cylinder circumference to the rear stagnation point, the water surface level gradually increases, reaching the highest level at the rear stagnation point. In the presence of the cylinder, due to wave scattering from wave-cylinder interactions, significant wave run-up is observed on the front side, with the highest run-up at the stagnation point. The largest discrepancies between the wave run-up and the undisturbed wave elevation result in the greatest positive scattering pressure around the azimuth of 0° near the undisturbed water level, corresponding to the positive SFL region above the naturally evolved negative SFL region in figure 11(a). On the rear side, pronounced wave set-down symmetrically occurs at azimuths of -40° and 40° , inducing significant negative scattering pressure regions around the water's surface, over the naturally evolved positive scattering pressure regions underwater due to the arrival of the main crest.

From 15.30 to 15.45 s, the wave run-up has receded, and no significant positive scattering pressure is observed in figure 12(B-f); most regions are close to zero scattering pressure. The wave set-down on the rear side in figure 12(B-r) continues to evolve and extends from around -40° and 40° to the front shoulders of the cylinder, continuing to induce significant negative scattering pressure at the wave surface level, corresponding to the peak value of 'positive insertion' around Z=0 m in figure 11(b).

At 15.60 s, as the main crest has not completely passed the cylinder, the undisturbed wave elevations still follow the same pattern as at time points a and b. However, wave elevations with the cylinder's presence change significantly. Wave set-down can be observed on the front side in figure 12(C-f), inducing a large negative scattering pressure region. In figure 12(C-r), wave run-up occurs and induces a positive scattering pressure region from -60° to 60° , while around the shoulders of the cylinder, the negative regions are influenced by the wave set-down from the front side.

3.4. Spectral decomposition

Building on the foundation laid by Stokes-type harmonic series theory (Stokes 1847), which applies to both harmonic and wave steepness in the free-surface elevation and horizontal wave forces of focused wave groups, Zang *et al.* (2006) and Chen *et al.* (2018) effectively isolated higher harmonics in their studies using a two-phase-decomposition method. This approach facilitated the distinct separation of odd and even harmonics within time histories. To enhance the separation of harmonics, Fitzgerald *et al.* (2014) introduced a four-phase method. This advanced method allows better separation using two additional force signals by implementing further phase shifts in the linear paddle signal, requiring four distinct runs for each test case. Each run generates wave groups with the same paddle signal, albeit with the phase of each linear Fourier component shifted by 0° , 90° , 180° and 270° , yielding four respective force time histories: F_0 , F_{90} , F_{180} and F_{270} . Here, we adopt the four-phase method to extract individual high-order harmonic Stokes-type

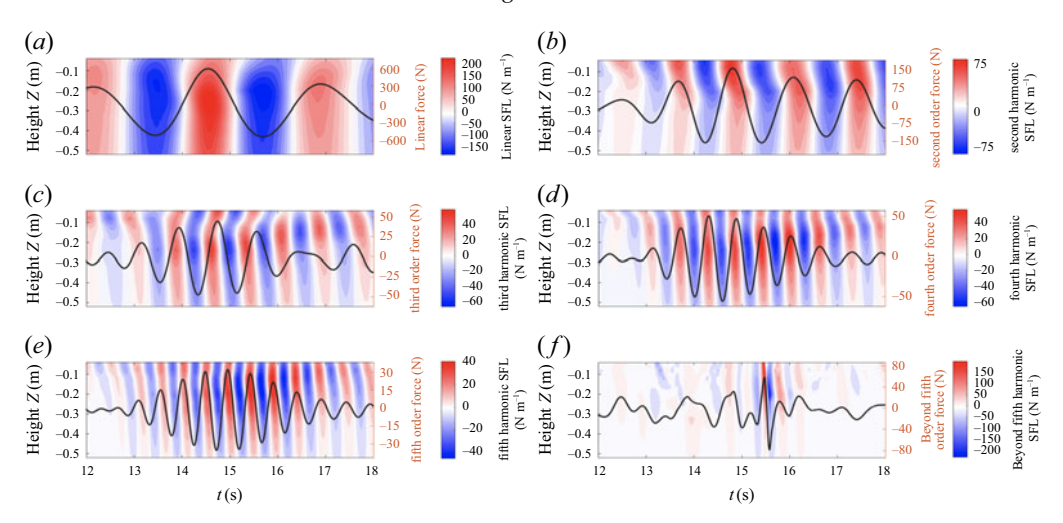


Figure 13. Contour plot of inline SFL against vertical level relative to still water level and time, with overlaying time histories of individual harmonic forces (black line) decomposed by spectral decomposition for (a) the linear harmonic, (b) the second harmonic, (c) the third harmonic, (d) the fourth harmonic, (e) the fifth harmonic and (f) beyond the fifth harmonic.

components. The required linear combinations of these four phase-shifted runs are as follows:

$$\frac{1}{4} \left(F_0 - F_{90}^H - F_{180} + F_{270}^H \right) = \left(A f_{11} + A^3 f_{31} + A^5 f_{51} \right) \cos \varphi + A^5 f_{55} \cos 5\varphi + O(A^7)
\frac{1}{4} \left(F_0 - F_{90} + F_{180} - F_{270} \right) = \left(A^2 f_{22} + A^4 f_{42} \right) \cos 2\varphi + O(A^6)
\frac{1}{4} \left(F_0 + F_{90}^H - F_{180} - F_{270}^H \right) = \left(A^3 f_{33} + A^5 f_{53} \right) \cos 3\varphi + O(A^7)
\frac{1}{4} \left(F_0 + F_{90} + F_{180} + F_{270} \right) = A^2 f_{20} + A^4 f_{40} + A^4 f_{44} \cos 4\varphi + O(A^6).$$
(3.1)

In this sequence, the combinations are devised to isolate the linear (first harmonic), the second harmonic sum, the third harmonic sum and ultimately, both the second harmonic difference and the fourth harmonic sum terms separated by frequency filtering. Here, A is the linear wave amplitude, the coefficients f_{mn} conceptually represent the wave-to-force transfer functions. Additionally, the expression $\varphi = \omega t + \varphi_0$ specifies the phase of the linear component of the incident wave, with a predetermined phase shift φ_0 .

In this study, we use the phase-decomposition method to examine the vertical distribution of scattering forces, scattering wave elevations and scattering pressure. The spectral decomposition results of the SFL are illustrated in figure 13, aligned with the time histories of each corresponding ordered harmonic inline force, depicted in black lines. Our discussion is confined purely to water-induced hydrodynamic forces, with a specific focus on the secondary load cycles. Therefore, we only consider the SFL below the still water level in figure 13. Notably, all crests of force curves align within the positive region in the SFL, and troughs fall within the negative region. This pattern indicates that the time histories of individual high-order forces exhibit an excellent correlation with their respective high-order harmonic SFLs. Such alignment underscores the spectral decomposition method's effectiveness in segregating the vertical distributions of SFL.

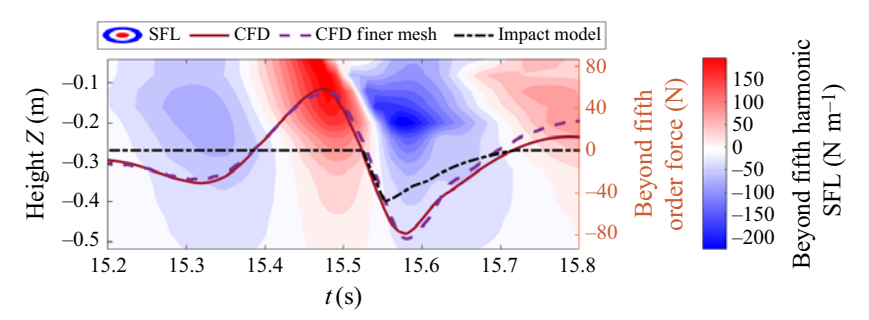


Figure 14. Beyond the fifth harmonic SFL, comparing CFD simulation results, refined CFD simulations with a finer mesh and the impact force model results for rear-side quasi-impulsive force from Tang *et al.* (2024).

As the harmonic order increases from the first to the fifth, the oscillations between positive and negative regions in the SFL contour plots become progressively more rapid, while the magnitudes of these harmonic SFL components generally decrease. Despite this decreasing trend, the nonlinear contributions remain substantial compared with the linear SFL, underscoring their significance within the overall SFL.

Remarkably, harmonics beyond the fifth order display significant magnitudes, with negative regions (-224 N m^{-1} in figure 13f) surpassing the linear SFL (-178 N m^{-1} in figure 13a), indicative of a pronounced negative region in the SFL and a violent quasi-impulsive force at the trough in the total force curve aforementioned in figure 10. The distinct positive region around 15.45 s, aligning with the 'positive insertion', is also notable.

To ensure that these significant high-order harmonics are physical rather than artefacts from mesh resolution, figure 14 cross-checks the beyond-fifth-order forces using simulations with two mesh resolutions: one with a local horizontal mesh size of L/700 (based on convergence tests in Chen *et al.* (2014)) and another with a finer mesh size of L/1050. The forces associated with the 'positive insertion' and the violent quasi-impulsive force from the rear side agree well between the two resolutions. This consistency confirms mesh convergence and rules out the possibility that these results are caused by numerical noise or insufficient mesh refinement. Consequently, a significant push-and-pull force is verified as being physically induced by the secondary load cycle.

This push-and-pull force depicted in figure 14 is hypothesised to be initiated by the suction caused by wave set-down at the cylinder's rear side. The pull force echoes findings from our previous work (Tang *et al.* 2024), where it was identified as a quasi-impulsive force originating from the rear side. To further explore this similarity, an impact model was utilised to predict this force, highlighting its resemblance to frontal impact forces. We applied a commonly used breaking wave model proposed by Goda (1966)

$$F_I(t) = \lambda \eta_b C_s \rho R c^2 \left(1 - \frac{c}{R} t \right). \tag{3.2}$$

Following the methodology in Tang *et al.* (2024), for this wave condition, we select a wave curling factor $\lambda = 0.4$, a peak impact crest height $\eta_b = 0.19$ m, an impact coefficient $C_s = \pi$ and a wave celerity c = 1.14 m·s⁻¹. The backward impact force calculated by this model, as shown in figure 14, accurately captures the duration of the impact. Although the force magnitudes show discrepancies (likely because the coefficient C_s is empirically derived from physical tests where the cylinder is not perfectly rigid as assumed in the CFD model), the similarity between the pull force and typical frontal impact force is evident.

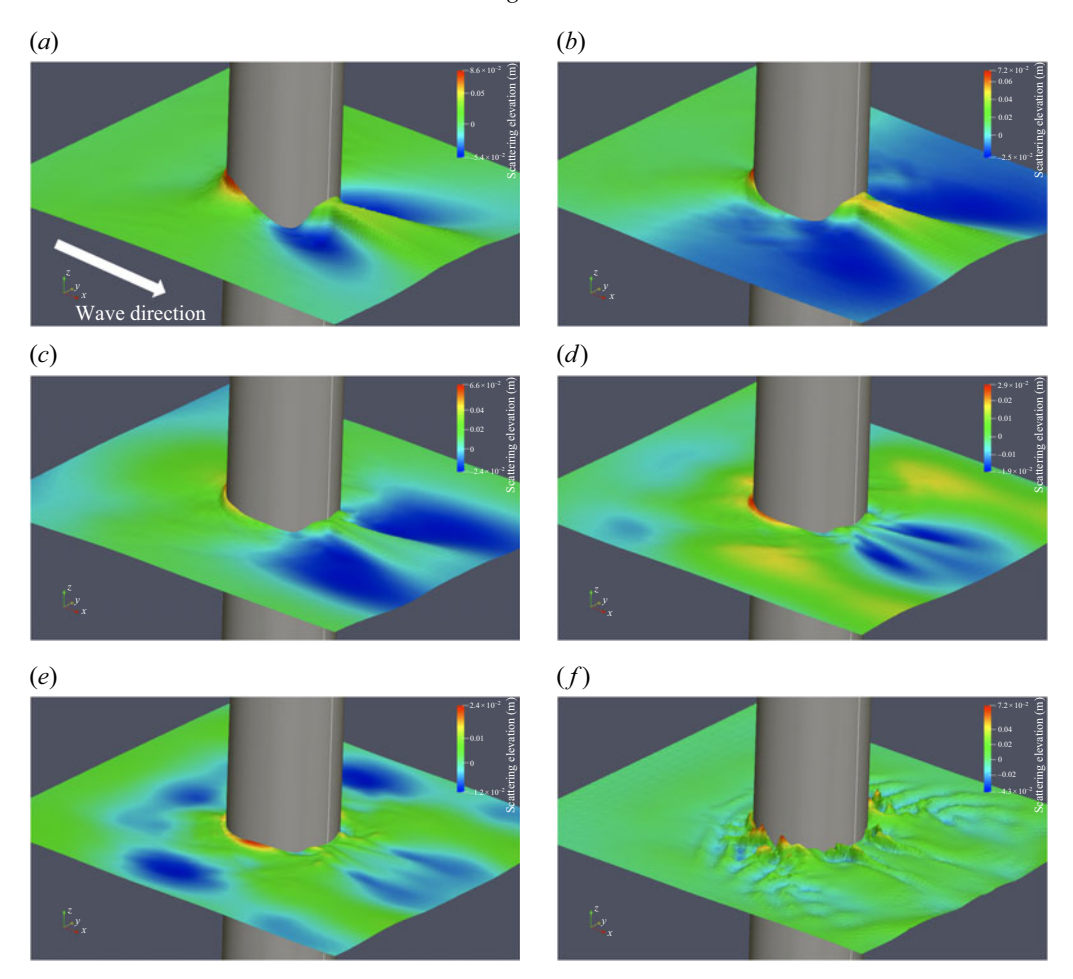


Figure 15. Scattering wave field at time point a (15.30 s), illustrating (a) the linear harmonic, (b) the second harmonic, (c) the third harmonic, (d) the fourth harmonic, (e) the fifth harmonic and (f) harmonics beyond the fifth. (Colour bar: scattering elevation (m).)

This confirms that the pronounced negative region in the SFL indeed corresponds to a backward quasi-impulsive impact phenomenon.

These push-and-pull forces play a crucial role in the trough oscillations of the total force curve associated with the secondary load cycle. Nevertheless, the initiation of the secondary load cycle, presumed to be triggered by the suction effect of wave set-down on the cylinder's rear side, is not directly discernible from the SFL beyond the fifth harmonics alone. The subsequent scattering wave fields of each individual harmonic, as presented in figures 15 and 16, provide further evidence on how these harmonics contribute to initiating the secondary load cycle.

Figures 15, 16 and 17 depict the scattering wave field around the cylinder from the linear components up to the fifth harmonics, as well as harmonics beyond the fifth at 15.30, 15.45 and 15.60 s, respectively. Supplementary movies of the harmonic-resolved free-surface evolution from 12 to 18 s are available at https://doi.org/10.1017/jfm.2025.10738 (Movies 2–7 correspond to the linear harmonic, the second harmonic, the third harmonic, the fourth harmonic, the fifth harmonic and harmonics beyond the fifth, respectively). As discussed in § 3.2, the frontal wave run-up, even in its set-down phase at 15.30 s, combined with the

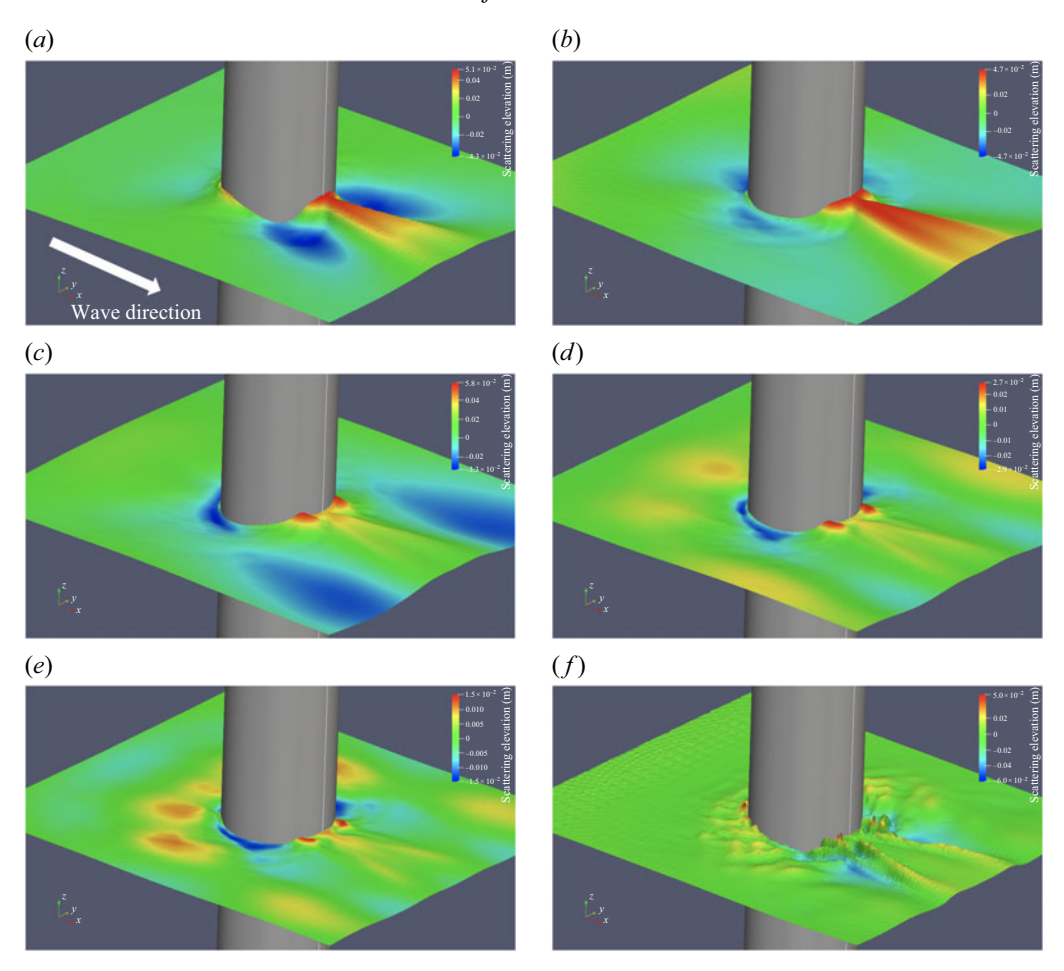


Figure 16. Scattering wave field at time point b (15.45 s), illustrating (a) the linear harmonic, (b) the second harmonic, (c) the third harmonic, (d) the fourth harmonic, (e) the fifth harmonic and (f) harmonics beyond the fifth. (Colour bar: Scattering elevation (m).)

suction effect of wave set-down at the cylinder's rear, contributes to the positive region near the free surface in the SFL shown in figure 10. And this positive region in the SFL is inferred to initiate the secondary load cycle. In figure 15, frontal wave run-up is evident across all harmonics. However, the wave set-down at the cylinder's rear, visible from the linear through the fifth harmonics, evolves at different speeds for different harmonics. This causes set-down regions in certain harmonics, such as the fourth and fifth, to drift away from the cylinder. Collectively, these observations suggest that all harmonics play a part in contributing to the positive SFL near the free surface, potentially initiating the secondary load cycle.

By 15.45 s, as depicted in figure 16, different harmonics of scattering waves exhibit distinct behaviours due to their varying evolution speeds. Despite expectations that scattering waves provide positive inline forces around this moment, the second harmonic, for instance, exhibits wave run-up at the cylinder's rear and set-down at the front, while wave set-down regions at the rear have disappeared. This pattern suggests negative inline forces from the second harmonic, consistent with the second harmonic SFL shown in figure 13(b). Conversely, harmonics beyond third, identified as contributors to the

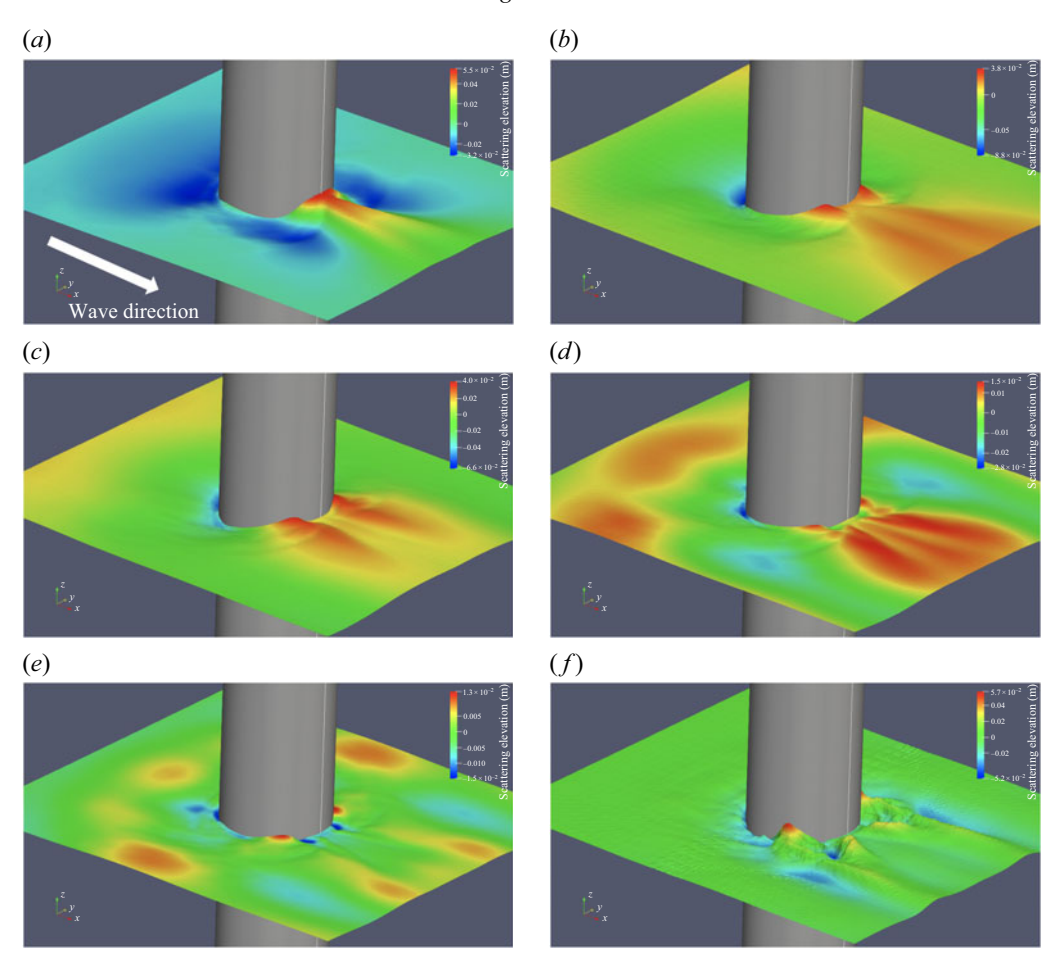


Figure 17. Scattering wave field at time point c (15.60 s), illustrating (a) the linear harmonic, (b) the second harmonic, (c) the third harmonic, (d) the fourth harmonic, (e) the fifth harmonic and (f) harmonics beyond the fifth. (Colour bar: scattering elevation (m).)

'positive insertion', still exhibit wave set-down regions at the cylinder's rear, suggesting the potential for generating positive inline forces. Nonetheless, since the peak of the 'positive insertion' occurs beneath the free surface, the free-surface profiles of harmonics beyond fifth appear spiky and indicate localised splashing phenomena rather than significantly contributing to positive inline forces.

Figure 17 at 15.60 s shows that, despite discrepancies in evolution speed, all harmonics exhibit a wave set-down at the cylinder's front and wave run-ups at the rear simultaneously. At this time point, the collective effect of different harmonics results in negative inline forces, leading to a pronounced negative region in the SFL and a quasi-impulsive force at the trough in the total force curve.

Decomposed scattering pressures in the azimuthal distribution at time points a (15.30 s), b (15.45 s) and c (15.60 s) are shown in figure 18. Due to the symmetric nature of the azimuthal scattering pressure observed in figure 12, the decomposed azimuthal scattering pressure is only presented for one half of the cylinder circumference. The front stagnation point is at 0° and the azimuthal angle increases counterclockwise to 180° at the rear stagnation point.

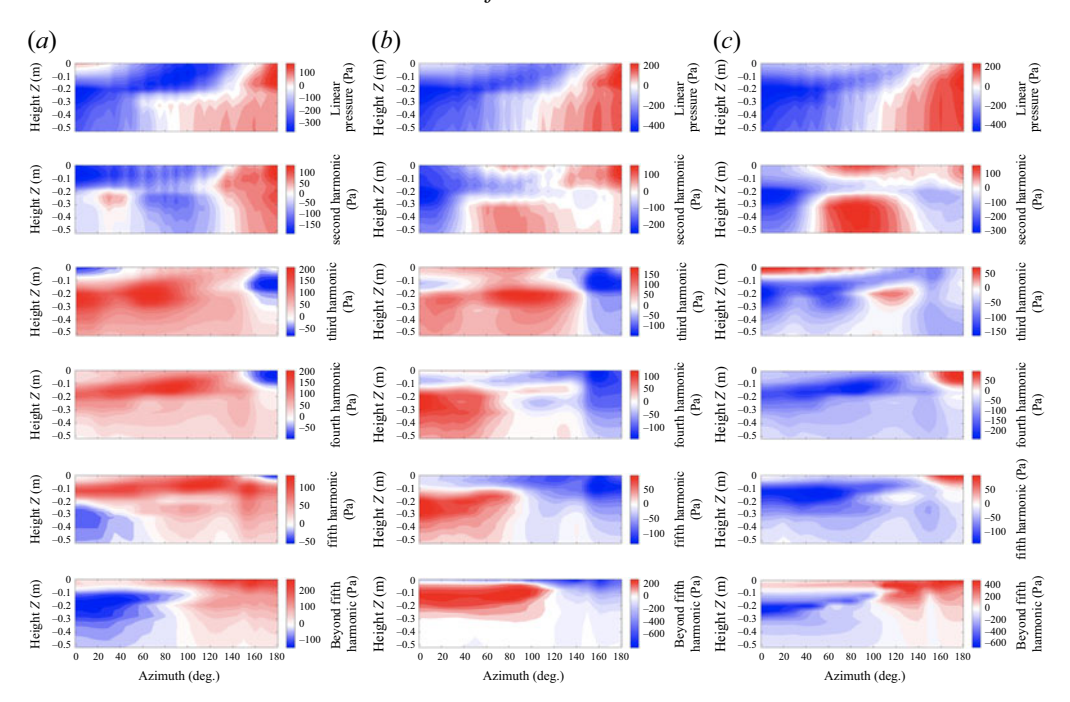


Figure 18. Contour plot of scattering pressure against cylinder height and azimuth at (a) time point a (15.30 s), (b) time point b (15.45 s) and (c) time point c (15.60 s) decomposed by spectral decomposition for different harmonics.

At 15.30 s, the initiation of the secondary load cycle is linked to the negative SFL region induced by the suction effect of the wave set-down from the rear side of the cylinder. In figure 18(a), it is evident that the negative scattering pressure from the rear of the cylinder is primarily contributed by the third, fourth and fifth harmonics around the rear stagnation point, ranging from 160° to 180° . Additionally, in the linear harmonic, negative scattering pressure is observed around the shoulder of the cylinder, ranging from 60° to 120° . The positive scattering pressure at the front stagnation point in the linear harmonic also contributes to the initiation of the secondary load cycle.

By 15.45 s, harmonics beyond the fifth harmonic in figure 18(b) begin to contribute to the positive SFL, with very large negative scattering pressure from the rear side ranging from 120° to 180° around Z = 0 m, and positive pressure from the front side ranging from 0° to 100° around Z = -0.15 m, together inducing the 'positive insertion'.

At 15.60 s, all harmonics in figure 18(c) show negative scattering pressure on the front side and positive scattering pressure on the rear side, resulting in a subsequently very large negative SFL. The harmonics beyond the fifth harmonic exhibit the largest magnitudes of positive and negative pressure.

From the azimuthal scattering pressure, it is evident that each nonlinear individual harmonic from the second to the fifth order has a pronounced value relative to the linear harmonic. The harmonics beyond the fifth harmonic demonstrate the most significant magnitudes of both positive and negative scattering pressure. Particularly, as the azimuthal scattering pressure field in figure 18(b) transitions to that in figure 18(c), local areas around Z = -0.15 m on the front side and around Z = 0 m on the rear side experience a rapid shift from large positive/negative pressure to large negative/positive pressure. In long-term steep sea states, with multiple occurrences of secondary load cycles, higher-order harmonics may significantly impact the cumulative fatigue damage of local structural elements.

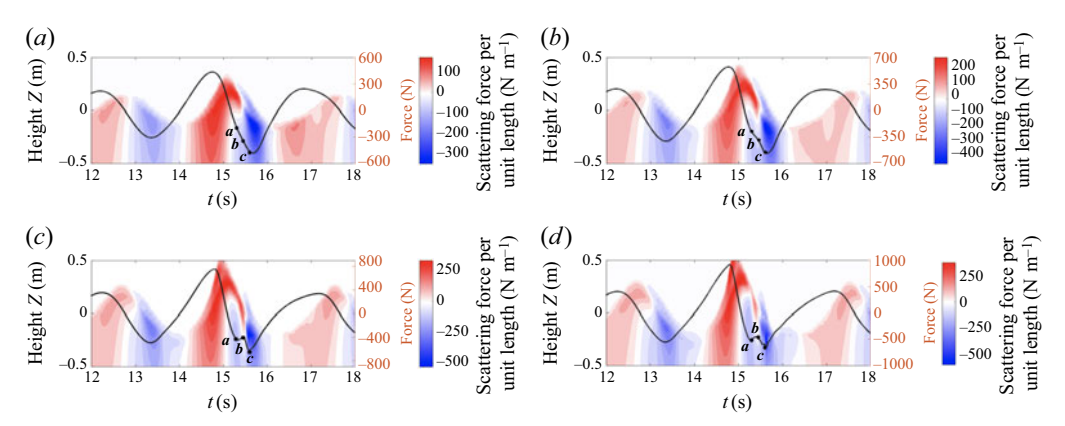


Figure 19. Contour plot of inline SFL against vertical level relative to still water level and time, with overlaying time histories of total force (black line) for the incident waves ($k_p = 0.73 \text{ m}^{-1}$) and cylinder slenderness $k_p R = 0.15$ with varying amplitudes: (a) $\eta_c = 0.24 \text{ m}$, $k_p \eta_c = 0.18$, (b) $\eta_c = 0.34 \text{ m}$, $k_p \eta_c = 0.25$, (c) $\eta_c = 0.41 \text{ m}$, $k_p \eta_c = 0.30$ and (d) $\eta_c = 0.47 \text{ m}$, $k_p \eta_c = 0.34$. Critical time points a (15.30 s), b (15.45 s) and c (15.60 s) are highlighted.

4. Influence of wave steepness

This section compares test cases with varying main crest wave amplitudes to investigate how different incident wave amplitudes influence the nonlinear wave forces and the secondary load cycle.

4.1. Scattering force per unit vertical length

Figure 19 presents the SFL alongside the total force–time histories for incident waves with a constant wavenumber $(k_p = 0.73 \text{ m}^{-1} \text{ corresponding to } k_p R = 0.15)$ but varying main crest wave amplitudes. As observed, with increasing wave steepness, $k_p \eta_c$, the main crest of the total force curves in figures 19(a) and 19(b) transitions from relatively smooth to markedly sharper, indicating a nonlinear impulsive force at the cylinder's front. This effect is mirrored in the SFL, where the vertical distribution of the positive region ascends higher around 15 s. Specifically, for $k_p \eta_c = 0.18$ and 0.25, the positive region's maximum height Z reaches approximately 0.36 and 0.44 m, respectively. Conversely, for $k_p \eta_c = 0.30$ and 0.34, the positive region extends over 0.5 m, signifying elevated wave run-up at the cylinder front. Notably, at the highest wave steepness $(k_p \eta_c = 0.34)$, the peak positive region in the SFL around 15 s reaches 429 N/m, significantly exceeding the values observed at lower steepness levels (197 N m₋₁ when $k_p \eta_c = 0.18$, 272 N m₋₁ when $k_p \eta_c = 0.25$ and 354 N m₋₁ when $k_p \eta_c = 0.30$).

The first trough following the main crest in the total force curve depicted in figure 19(a) does not exhibit significant nonlinearity for $k_pR=0.15$, $k_p\eta_c=0.18$. However, as $k_p\eta_c$ increases to 0.25 in figure 19(b), changes in the curve's slope reveal noticeable nonlinearity. Between points a and b, the slope is visibly reduced, yet the force tendency does not shift to positive, unlike in the scenarios with $k_p\eta_c=0.30$ and 0.34. In the SFL, the emergence of the 'positive insertion' begins at $k_p\eta_c=0.18$ but does not fully develop, leading to subtle slope variations in the total force curve. When $k_p\eta_c$ reaches 0.25, the 'positive insertion' becomes more pronounced, aligning with the observed slope change in the total force curve, indicative of the secondary load cycle. As $k_p\eta_c$ increases to 0.30, the peak of the 'positive insertion' rises to 294 N m⁻¹, approaching the magnitude of the positive region induced by impulsive wave forces at the front. Yet, when $k_p\eta_c$ escalates to 0.34, the peak value diminishes to 211 N m⁻¹.

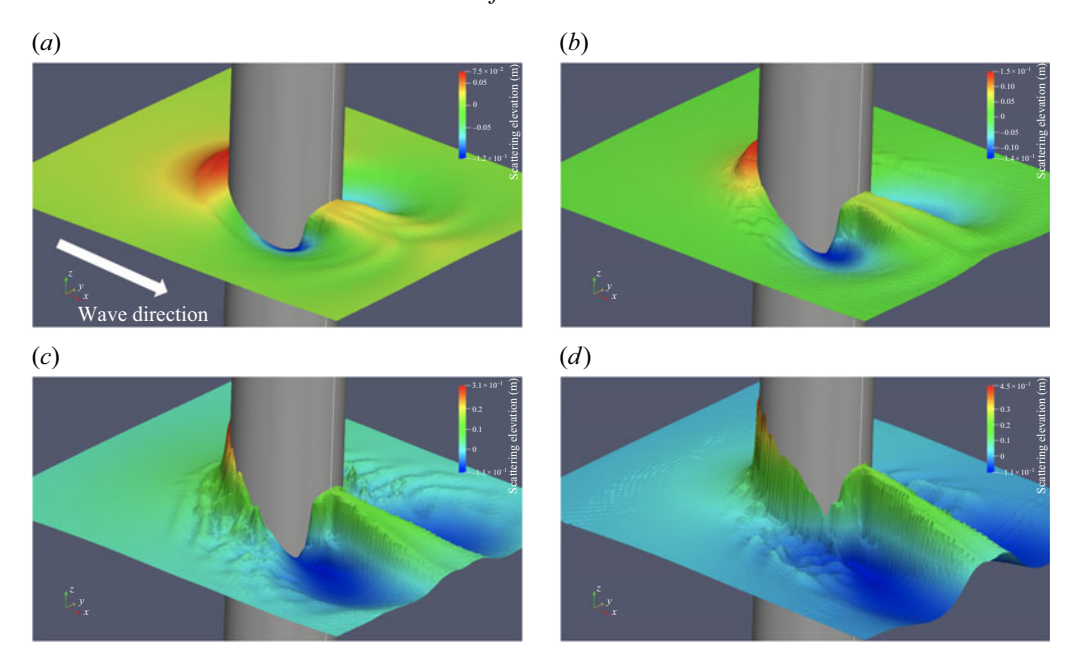


Figure 20. Scattering wave field at time point a (15.30 s) for the incident waves ($k_p = 0.73 \text{ m}^{-1}$) and cylinder slenderness $k_p R = 0.15$ with varying amplitudes: (a) $\eta_c = 0.24$ m, $k_p \eta_c = 0.18$, (b) $\eta_c = 0.34$ m, $k_p \eta_c = 0.25$, (c) $\eta_c = 0.41$ m, $k_p \eta_c = 0.30$ and (d) $\eta_c = 0.47$ m, $k_p \eta_c = 0.34$. (Colour bar: scattering elevation (m).)

Supplementary movies showing the scattering free-surface evolution from 12 to 18 s are available at https://doi.org/10.1017/jfm.2025.10738 (Movies 8, 9, 1 and 10 correspond to η_c of 0.24, 0.34, 0.41 and 0.47 m, respectively). At times a (15.30 s) and b (15.45 s), the wave set-down at the cylinder's rear side, contributing to suctions that likely initiate the secondary load cycle as discussed in § 3.2, evolves differently across wave steepness levels, as shown in figures 20 and 21. At $k_p R = 0.15$, $k_p \eta_c = 0.18$, the wave set-down is minimal, correlating with an underdeveloped 'positive insertion'. As $k_p \eta_c$ increases to 0.30, the wave set-down's evolution is more pronounced. However, the evolution of the wave set-down at the rear shoulders of the cylinder when $k_p \eta_c = 0.34$ is not as complete as $k_p \eta_c = 0.30$, potentially due to rapid over-washing from wave run-up observed in figures 20(d) and 21(d). Physical experiments at KHL show this phenomenon (figure 22), where high wave celerity at steep waves ($k_p \eta_c = 0.40$) results in rapid wave run-up, propagating surrounding the cylinder surface and impacting wave set-down evolution.

For the troughs in the total force curve, the scenarios with $k_p\eta_c=0.18$ and 0.25 feature smooth curves. Conversely, the cases with $k_p\eta_c=0.30$ and 0.34 exhibit sharp troughs akin to the crests, suggesting quasi-impulsive forces from the cylinder's rear, as discussed in § 3. With increasing $k_p\eta_c$, the magnitude of the negative area following the 'positive insertion' in the SFL escalates. This trend aligns with observations from the scattering fields depicted in figure 23, With an increase in $k_p\eta_c$, the wave set-down in front of the cylinder deepens, with the lowest level of free surface transitioning from -0.086 m at $k_p\eta_c=0.18$ to -0.2 m at $k_p\eta_c=0.34$. Simultaneously, the wave run-up at the cylinder's rear elevates, with the highest level of free surface rising from 0.069 m at $k_p\eta_c=0.18$ to 0.11 m at $k_p\eta_c=0.34$. This dynamics collectively enhances the magnitude of the negative areas in the SFL. Specifically, for $k_p\eta_c=0.34$, the deepest negative value reaches -600 N m⁻¹, surpassing the -531 Nm⁻¹ observed with $k_p\eta_c=0.30$. Notably, across all four cases,

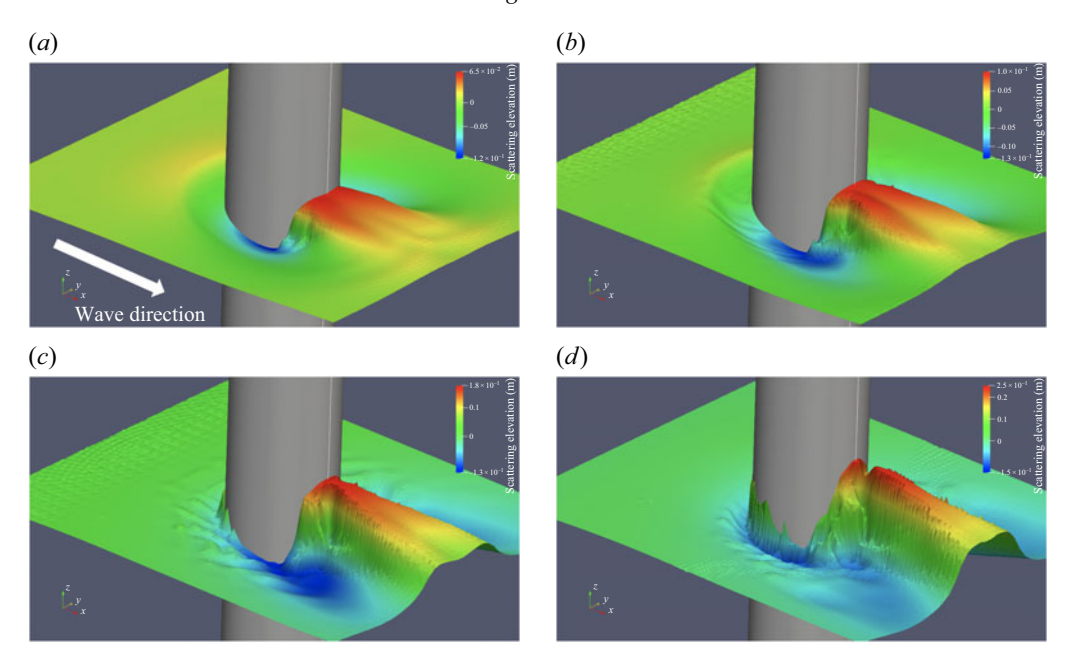


Figure 21. Scattering wave field at time point b (15.45 s) for the incident waves ($k_p = 0.73 \text{ m}^{-1}$) and cylinder slenderness $k_p R = 0.15$ with varying amplitudes: (a) $\eta_c = 0.24 \text{ m}$, $k_p \eta_c = 0.18$, (b) $\eta_c = 0.34 \text{ m}$, $k_p \eta_c = 0.25$, (c) $\eta_c = 0.41 \text{ m}$, $k_p \eta_c = 0.30$ and (d) $\eta_c = 0.47 \text{ m}$, $k_p \eta_c = 0.34$. (Colour bar: scattering elevation (m).)

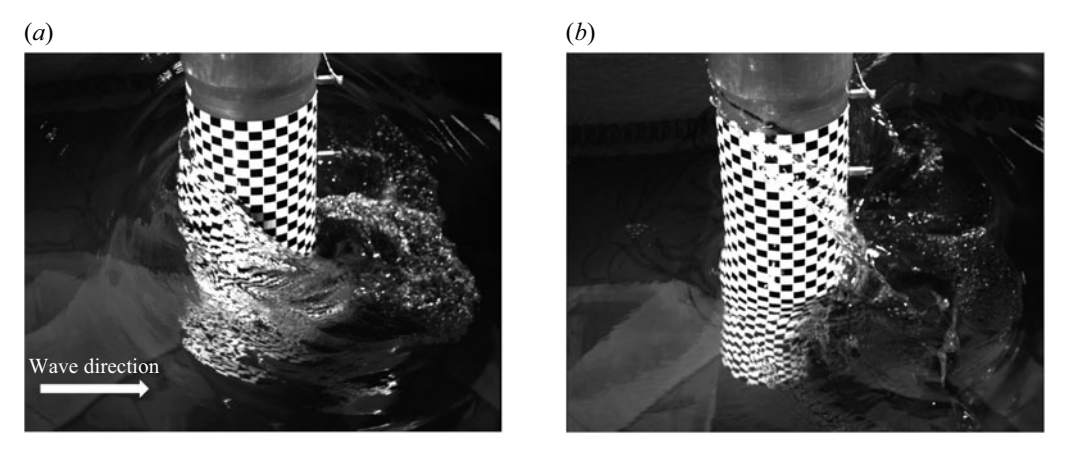


Figure 22. High-speed camera images from the KHL experimental tests showing interactions between the cylinder and incident waves with (a) $k_p R = 0.15$, $k_p \eta_c = 0.3$ and (b) $k_p R = 0.15$, $k_p \eta_c = 0.4$.

the peak magnitudes of negative areas downstream significantly exceed those of the upstream positive areas, a phenomenon not easily discerned from the total force analysis.

4.2. Spectral decomposition

Spectral decomposition obtains each individual harmonic SFL below the still water level, from the linear to the fifth harmonics, across cases with varying wave steepness ($k_p \eta_c = 0.25$, 0.30 and 0.34), as depicted in figure 24. It is observed that the peak values of both positive and negative areas in the SFL from the linear to the fourth harmonics generally remain consistent, particularly for cases with $k_p \eta_c = 0.30$ and 0.34. Despite an

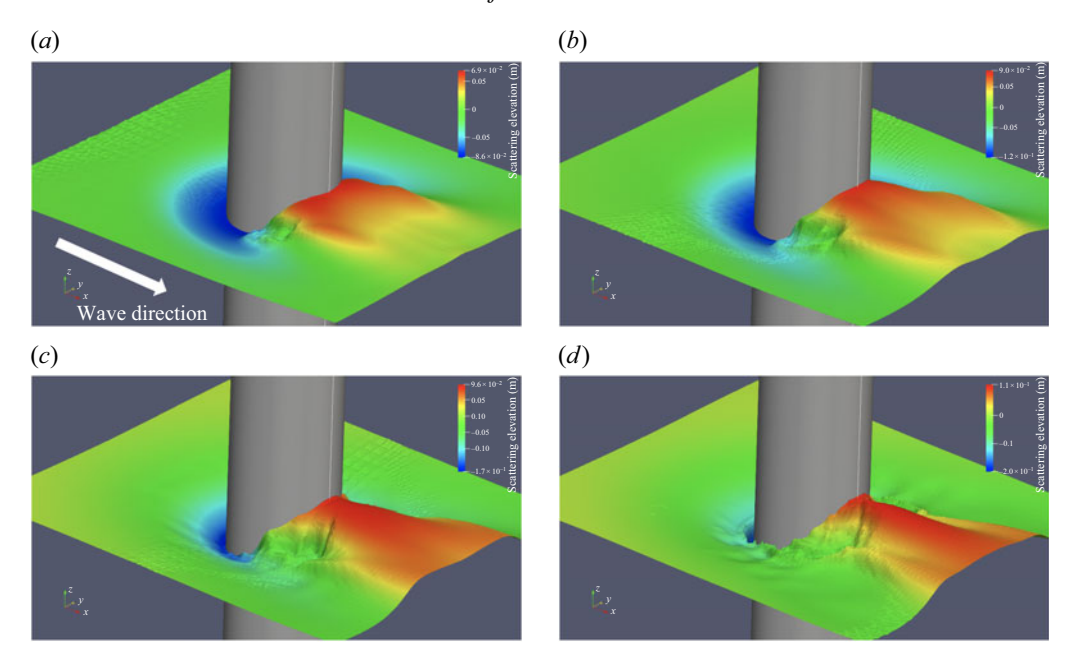


Figure 23. Scattering wave field at time point c (15.60 s) for the incident waves ($k_p = 0.73 \text{ m}^{-1}$) and cylinder slenderness $k_p R = 0.15$ with varying amplitudes: (a) $\eta_c = 0.24 \text{ m}$, $k_p \eta_c = 0.18$, (b) $\eta_c = 0.34 \text{ m}$, $k_p \eta_c = 0.25$, (c) $\eta_c = 0.41 \text{ m}$, $k_p \eta_c = 0.30$ and (d) $\eta_c = 0.47 \text{ m}$, $k_p \eta_c = 0.34$. (Colour bar: scattering elevation (m).)

increase in wave steepness, the impact on the SFL from the linear to the fourth harmonics is minimal. The fifth harmonic SFL, however, exhibits a slight increase with the wave steepness. Overall, the sensitivity of the first five harmonic SFLs to changes in wave steepness is minimal under the still water level.

In contrast, the SFL beyond the fifth harmonic, presented in figure 25, exhibits a marked variation with changing $k_p\eta_c$, directly correlating to the occurrence of oscillations and quasi-impulsive forces at the trough of the total force curves in figure 19, associated with the secondary load cycle. Among the three SFLs with differing $k_p\eta_c$, the largest positive area, associated with the 'positive insertion', occurs at $k_p\eta_c=0.30$, aligning with observations in § 4.1. The $k_p\eta_c=0.34$ case exhibits the highest magnitude of negative area, accompanied by pronounced oscillations in the beyond fifth harmonic SFL, as shown in figure 21(c). Table 1 lists the peak values of critical areas from figure 25, including their occurrence times and heights. Notably, as $k_p\eta_c$ increases, the 'positive insertion' peak values occur at deeper locations, from -0.04 to -0.12 m, with subsequent negative areas also appearing deeper. A significant positive area emerges after approximately 15.7 s, with relatively minor peak values for $k_p\eta_c=0.25$ and 0.30 compared with the 'positive insertion', but the $k_p\eta_c=0.34$ case shows an even greater peak value.

Figure 26 highlights a considerable wave run-up evolving between 15.75 and 15.95 s after the passage of the main crest for $k_p\eta_c=0.30$ and 0.34, potentially driven by the wave diffraction of the wave run-up in the quasi-impulse phenomenon at the cylinder rear side (i.e. type-II wave from the rear side), as evidenced in figures 23(c) and 23(d), leading to a pronounced increase in positive SFL. Correspondingly, scattering waves beyond the fifth harmonics at 15.75 s in figure 27 illustrate a wave run-up at the cylinder front. The $k_p\eta_c=0.34$ scenario showcases a larger wave run-up, indicating a significant positive area from a double oscillation, albeit with a substantially higher peak value in the beyond fifth harmonic SFL. Given that the peak value appears below the still water level at

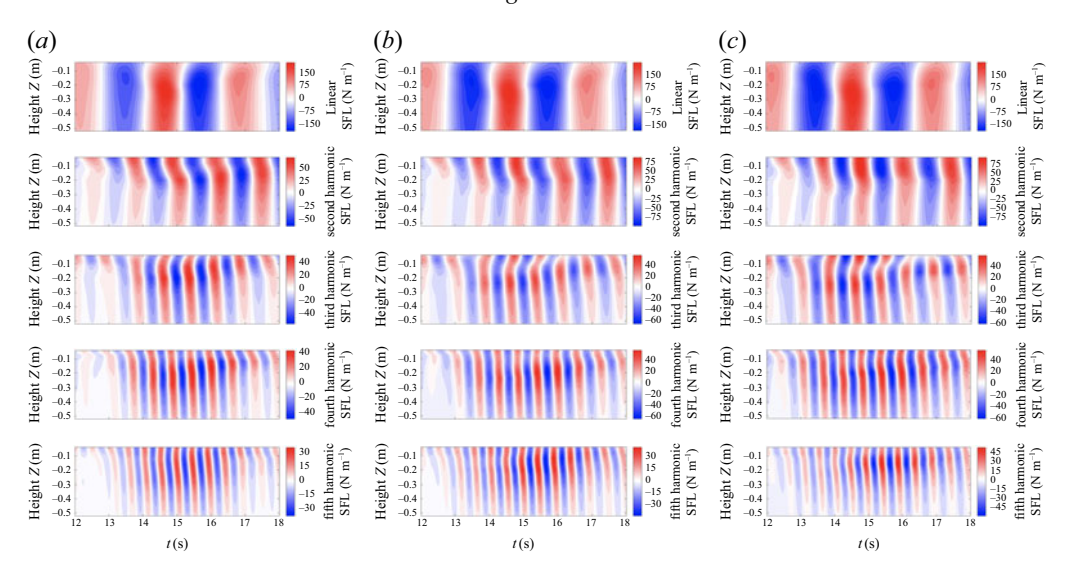


Figure 24. Contour plot of inline SFL against vertical level relative to still water level and time, obtained through spectral decomposition for the linear, second, third, fourth and fifth harmonics across cases with cylinder slenderness $k_p R = 0.15$ and varying wave steepness: (a) $k_p \eta_c = 0.25$, (b) $k_p \eta_c = 0.30$ and (c) $k_p \eta_c = 0.34$.

| Results from figure 25 | | | | |
|------------------------|---|--|-------------------------------|-------------------------------|
| $k_p \eta_c$ | Areas in beyond fifth harmonic SFL | Peak value | Occurrence time | Height Z |
| 0.25 | 'positive insertion' Subsequent negative area The second pronounced positive area | 71 N m ⁻¹ -136 N m-1 53 N m-1 | 15.45 s 15.59 s 15.79 s | -0.04 m -0.12 m -0.12 m |
| 0.30 | 'positive insertion' Subsequent negative area The second pronounced positive area | 209 N m-1 -224 N m-1 86 N m-1 | 15.47 s 15.57 s 15.79 s | -0.08 m -0.2 m -0.2 m |
| 0.34 | 'positive insertion' Subsequent negative area The second pronounced positive area | 114 N m-1 -277 N m-1 135 N m-1 | 15.44 s 15.63 s 15.75 s | -0.12 m -0.28 m -0.12 m |

Table 1. Peak values of beyond fifth harmonic SFL across different wave steepness for cylinder slenderness $(k_p R)$ of 0.15.

-0.12 m, it remains unseen from the scattering wave surface. This analysis, based on the spectral decomposed vertical distribution of scattering forces, brings to light a previously unobserved phenomenon: very high frequency (over fifth harmonic and order) oscillations could potentially influence structural fatigue. We note that such a loading component would be difficult to accurately record in a physical experiment because of the required structural stiffness.

5. Conclusions

This study provides a comprehensive examination of the nonlinear forces arising from severe wave interactions with vertical cylinder structures, integral to the design of

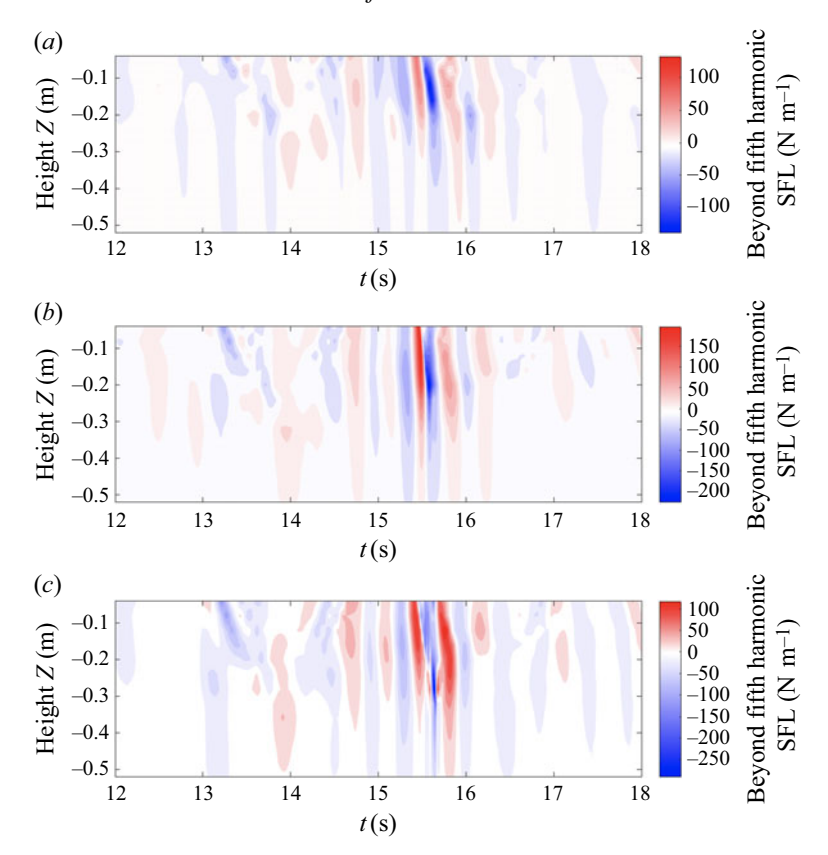


Figure 25. Contour plot of inline SFL against vertical level relative to still water level and time, obtained through spectral decomposition for the harmonics beyond fifth across cases with cylinder slenderness $k_p R = 0.15$ and varying wave steepness: (a) $k_p \eta_c = 0.25$, (b) $k_p \eta_c = 0.30$ and (c) $k_p \eta_c = 0.34$.

the column and foundation for offshore wind turbines. Our detailed experimental tests highlight that the secondary load cycle occurs commonly in wave–cylinder interactions. The scattering wave field offers a direct view of the wave scattering regime associated with the secondary load cycle. In addition, the vertical distributions of the scattering force and azimuthal scattering pressure field quantitatively reveal the wave–cylinder interaction beneath the water's free-surface level, an insight uniquely achievable through CFD simulations. Moreover, by applying a phase-based harmonic separation method, we have successfully isolated and analysed the harmonic components of the inline scattering force's vertical distribution, scattering pressure and the scattering wave field. This approach has allowed us to accurately delineate individual harmonics and shed light on the complex mechanisms of nonlinear forces related to the secondary load cycle.

From the experimental mapping, cases exhibiting the secondary load cycles cluster towards larger wave steepness. On a Froude-number plot, all cases with Fr < 0.3 showed no secondary load cycle, whereas all cases with Fr > 0.45 exhibited an obvious secondary load cycle; in the transitional band 0.3 < Fr < 0.45, secondary load cycle occurrence was mixed. These observations were made under non-breaking focused waves. In addition to the uni-directional waves, secondary load cycles were further observed for directional seas, which are closer in form to large waves in the field.

We first examine the vertical distribution of inline and scattering forces, synchronised with the scattering wave field and scattering pressure field at key time points. These time

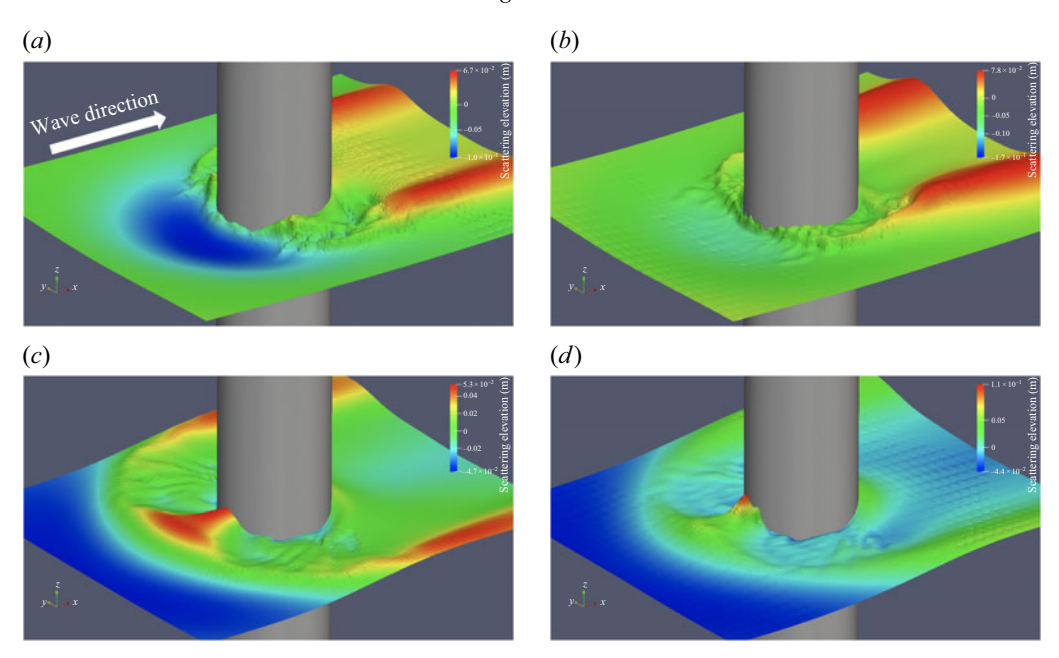


Figure 26. Scattering wave field at 15.75 s for the incident waves with (a) $k_p R = 0.15$, $k_p \eta_c = 0.30$, (b) $k_p R = 0.15$, $k_p \eta_c = 0.34$, and at 15.95 s for the incident waves with (c) k R = 0.15, $k_p \eta_c = 0.30$, (d) $k_p R = 0.15$, $k_p \eta_c = 0.34$. (Colour bar: scattering elevation (m).)

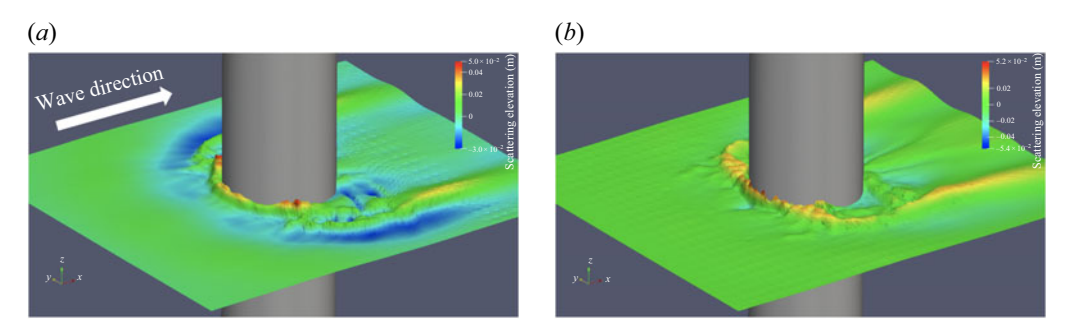


Figure 27. Scattering wave field beyond the fifth harmonic at 15.75 s for the incident waves with (a) $k_p R = 0.15$, $k_p \eta_c = 0.30$, (b) $k_p R = 0.15$, $k_p \eta_c = 0.34$. (Colour bar: scattering elevation (m).)

points highlight the onset of the oscillation associated with the secondary load cycle, the peak of the oscillation corresponding to the 'positive insertion' in the vertical force distribution, and the quasi-impulsive force at the trough corresponding to the subsequent significant negative area in the vertical force distribution. The insights gained from both above and below the water's free-surface level, along with the clear separation of each individual harmonic, indicate that the third, fourth and fifth harmonics play pivotal roles in providing a suction effect from the cylinder's rear side, contributing to the onset and evolution of the secondary load cycle. Higher harmonics beyond the fifth further exhibit rapid and significant value oscillations associated with a type-II wave from the rear side of the cylinder, inducing the 'positive insertion' and the backward quasi-impulsive force. These insights reveal the paramount importance of nonlinear forces within the secondary load cycle framework, offering novel perspectives on its mechanisms.

Notably, our analysis demonstrates that in certain wave regimes, nonlinear scattering forces exert a greater magnitude within the vertical force distribution than their linear counterparts. Additionally, the decomposed azimuthal scattering pressure indicates that higher-order harmonics beyond the fifth have potential to impact the cumulative fatigue damage of local structural elements due to large, rapid pressure shifts. These unique insights underscore the critical need to give greater consideration to the secondary load cycle in the design and assessment of offshore structures.

Building on this foundation, we further extend our exploration by comparing test cases across various wave steepness levels to assess their impact on nonlinear wave forces and the secondary load cycle. These new findings indicate that as wave steepness increases, high-order oscillations of the local scattering force become more pronounced and significant, potentially leading to a greater influence on structural fatigue damage. This observation, particularly regarding the pronounced discrepancies observed in harmonics beyond the fifth, underscores the intricate relationship between wave steepness and wave—cylinder interactions.

Together, these new findings enrich our understanding of the secondary load cycle and its governing mechanisms. By clarifying the significant role of nonlinear forces and the influence of wave steepness on these interactions, this research will contribute to the resilience and safety of offshore infrastructures in extreme maritime environments.

Supplementary movies. Supplementary movies are available at https://doi.org/10.1017/jfm.2025.10738.

Acknowledgement. This research is funded by EPSRC grant EP/V050079/1. Simulations are supported by EPSRC grant EP/X035751/1.

Declaration of interests. The authors report no conflict of interest.

REFERENCES

- ANTOLLONI, G., JENSEN, A., GRUE, J., RIISE, B.H. & BROCCHINI, M. 2020 Wave-induced vortex generation around a slender vertical cylinder. *Phys. Fluids* 32 (4), 042105.
- BALDOCK, T.E., SWAN, C. & TAYLOR, P.H. 1996 A laboratory study of nonlinear surface waves on water. *Philos. Trans. Royal Soc. A Math. Phys. Eng. Sci.* **354** (1707), 649–676.
- BOCCOTTI, P. 1983 Some new results on statistical properties of wind waves. Appl. Ocean Res. 5, 134-140.
- CHANG, S., HUANG, W., SUN, H. & LI, L. 2019 Numerical investigation of secondary load cycle and ringing response of a vertical cylinder. Appl. Ocean Res. 91, 101872.
- CHAPLIN, J.R., RAINEY, R.C.T. & YEMM, R.W. 1997 Ringing of a vertical cylinder in waves. *J. Fluid Mech.* 119–147.
- CHEN, L.F., ZANG, J., HILLIS, A.J., MORGAN, G.C.J. & PLUMMER, A.R. 2014 Numerical investigation of wave-structure interaction using openfoam. *Ocean Engine*. **88**, 91–109.
- CHEN, L.F., ZANG, J., TAYLOR, P.H., SUN, L., MORGAN, G.C.J., GRICE, J., ORSZAGHOVA, J. & RUIZ, M.T. 2018 An experimental decomposition of nonlinear forces on a surface-piercing column: Stokes-type expansions of the force harmonics. *J. Fluid Mech.* 848, 42–77.
- DING, HAOYU, et al. et al. 2025 Experimental investigation of nonlinear forces on a monopile offshore wind turbine foundation under directionally spread waves. J. Offshore Mechan. Arctic Engine. 147 (4), 042002.
- ESANDI, J.M., BULDAKOV, E., SIMONS, R. & STAGONAS, D. 2020 An experimental study on wave forces on a vertical cylinder due to spilling breaking and near-breaking wave groups. *Coast. Engine.* **162**, 103778.
- FITZGERALD, C.J., TAYLOR, P.H., EATOCK TAYLOR, R., GRICE, J. & ZANG, J. 2014 Phase manipulation and the harmonic components of ringing forces on a surface-piercing column. *Proc. R. Soc. A* **470** (2168), 20130847.
- GHADIRIAN, A. & BREDMOSE, H. 2019 Pressure impulse theory for a slamming wave on a vertical circular cylinder. J. Fluid Mech. 867, R1.
- GHADIRIAN, A. & BREDMOSE, H. 2020 Detailed force modelling of the secondary load cycle. *J. Fluid Mech.* 889, A21.
- GODA, Y. 1966 A study on impulsive breaking wave force upon a vertical pile. *Rept. Port Harbour Res. Inst.* **5** (6), 1–30.

- GRUE, J., BJØRSHOL, G. & STRAND, Ø. 1993 Higher harmonic wave exciting forces on a vertical cylinder. Preprint series. Mechanics and Applied Mathematics, Matematisk Institutt. Universitetet i Oslo.
- GRUE, J. & HUSEBY, M. 2002 Higher-harmonic wave forces and ringing of vertical cylinders. *Appl. Ocean Res.* **24** (4), 203–214.
- JACOBSEN, N.G., FUHRMAN, D.R. & FREDSØE, J. 2012 A wave generation toolbox for the open-source cfd library. Openfoam. Int. J. Numer. Meth. Fluids 70 (9), 1073–1088.
- LI, J., ZHANG, H., LIU, S., FAN, Y. & ZANG, J. 2022 Experimental investigations of secondary load cycle formation in wave force on a circular cylinder under steep regular waves. *Ocean Engine*. **253**, 111265.
- LINDGREN, G. 1970 Some properties of a normal process near a local maximum. *Annal. Math. Statist.* 41, 1870–1883.
- Lo, E. & MEI, C.C. 1985 A numerical study of water-wave modulation based on a higher-order nonlinear Schrödinger equation. J. Fluid Mech. 150, 395–416.
- LONGUET-HIGGINS, M.S., CARTWRIGHT, D.E. & SMITH, N.D. 1963 Observations of the Directional Spectrum of Sea Waves Using the Motions of Floating Buoy. InOcean Wave Spectra Prentice-Hall Inc
- PAULSEN, B.T., BREDMOSE, H., BINGHAM, H.B. & JACOBSEN, N.G. 2014 Forcing of a bottom-mounted circular cylinder by steep regular water waves at finite depth. *J. Fluid Mech.* 755, 1–34.
- RAINEY, R.C.T. 2007 Weak or strong nonlinearity: the vital issue. J. Eng. Math. 58 (1), 229-249.
- RIISE, B.H., GRUE, J., JENSEN, A. & JOHANNESSEN, T.B. 2018a High frequency resonant response of a monopile in irregular deep water waves. J. Fluid Mech. 853, 564–586.
- RIISE, B.H., GRUE, J., JENSEN, A. & JOHANNESSEN, T.B. 2018b A note on the secondary load cycle for a monopile in irregular deep water waves. *J. Fluid Mech.* **849**, R1.
- SHEIKH, R. & SWAN, C. 2005 Wave slamming on vertical surface-piercing cylinders: the role of nonlinear wave scattering, In Proc. ISOPE. OnePetro.
- STANSBERG, C.T. 1997 Comparing ringing loads from experiments with cylinders of different diameters an empirical study, In International Conference on the Behaviour of Offshore Structures, Delft (Netherlands), Jul 1997, 7–10.
- STOKES, G.G. 1847 On the theory of oscillatory waves. Trans. Camb. Phil. Soc. 8, 441-455.
- TANG, T., DING, H., DAI, S., TAYLOR, P.H., ZANG, J. & ADCOCK, T.A.A. 2024 An experimental study of a quasi-impulsive backwards wave force associated with the secondary load cycle on a vertical cylinder. *J. Fluid Mech.* **994**, A9.
- TROMANS, P., SWAN, C. & MASTERTON, S. 2006 Nonlinear potential flow forcing: the ringing of concrete gravity based structures. Health and Safety Executive Report.
- TROMANS, P.S., ANATURK, A.R. & HAGEMEIJER, P. 1991 A new model for the kinematics of large ocean waves-application as a design wave. In International Ocean and Polar Engineering Conference. vol. 17, pp. ISOPE–I–91–154.
- VON KARMAN, T. 1929 *The Impact On Seaplane Floats during Landing*. National Advisory Committee on Aeronautics, National Advisory Committee on Aeronautics.
- WAGNER, H. 1932 Uber stob-und gleitvorgange an der oberflache von flussigkeiten. Z. Angew. Math. Mech. 12, 193–215.
- YAN, M., MA, X., BAI, W., LIN, Z. & LI, Y. 2020 Numerical simulation of wave interaction with payloads of different postures using openfoam. *J. Mar. Sci. Engine.* 8 (6).
- ZANG, J., GIBSON, R., TAYLOR, P.H., EATOCK TAYLOR, R. & SWAN, C. 2006 Second order wave diffraction around a fixed ship-shaped body in unidirectional steep waves. *J. Offshore Mechan. Arctic Engine.* **128**, 89–99.
- ZANG, J., TAYLOR, P.H. & TELLO, M. 2010 Steep wave and breaking wave impact on offshore wind turbine foundations ringing re-visited. In 25th International Workshop On Water Waves and Floating Bodies.